HUBBLE SPACE TELESCOPE OBSERVATIONS OF GLOBULAR CLUSTERS IN M31 I: COLOR-MAGNITUDE DIAGRAMS, HORIZONTAL BRANCH METALLICITY DEPENDENCE, AND THE DISTANCE TO M31

Edward A. Ajhar, Carl J. Grillmair, Tod R. Lauer,
William A. Baum, S. M. Faber, Jon A. Holtzman,
Robert M. Light, Roger Lynds, and Earl J. O'Neil, Jr.

NOAO Preprint No. 681

Submitted to: *The Astronomical Journal*

November 1995

Hubble Space Telescope Observations of Globular Clusters in M31 I: Color-Magnitude Diagrams, Horizontal Branch Metallicity Dependence, and the Distance to M31[1]

Edward A. Ajhar
Kitt Peak National Observatory, National Optical Astronomy Observatories[2], P. O. Box 26732, Tucson, AZ 85726
Electronic mail: ajhar@noao.edu

Carl J. Grillmair
UCO/Lick Observatory, Board of Studies in Astronomy and Astrophysics, University of California, Santa Cruz, CA 95064
Electronic mail: carl@ucolick.org

Tod R. Lauer
Kitt Peak National Observatory, National Optical Astronomy Observatories[2], P. O. Box 26732, Tucson, AZ 85726
Electronic mail: lauer@noao.edu

William A. Baum
Department of Astronomy, Fm-20, University of Washington, Seattle, Washington 98195
Electronic mail: baum@astro.washington.edu

S. M. Faber
UCO/Lick Observatory, Board of Studies in Astronomy and Astrophysics, University of California, Santa Cruz, CA 95064
Electronic mail: faber@ucolick.org

Jon A. Holtzman
New Mexico State University, Box 30001, Dept. 4500, Las Cruces, NM 88003
Electronic mail: holtz@nmsu.edu

Robert M. Light
Infrared Processing and Analysis Center, California Institute of Technology, Pasadena, California 91125
Electronic mail: light@ipac.caltech.edu

Roger Lynds
Kitt Peak National Observatory, National Optical Astronomy Observatories[2], P. O. Box 26732, Tucson, AZ 85726
Electronic mail: rlynds@noao.edu

and

Earl J. O'Neil, Jr.
Kitt Peak National Observatory, National Optical Astronomy Observatories[2], P. O. Box 26732,
Tucson, AZ 85726
Electronic mail: oneil@noao.edu

ABSTRACT

This paper presents *Hubble Space Telescope* observations of four globular clusters in M31 with [Fe/H] ranging from −0.6 to −2.0. The Wide-Field and Planetary Camera-2 (WFPC-2) imaged these clusters through the F555W (V) and F814W (I) filters with total exposure times of 2000 s in each color. The ground-based spectroscopic metallicities are generally confirmed by the shapes of the red giant branches when compared to standard giant branches in V and I. In addition, two methods give similar reddening estimates for each cluster. The color-magnitude diagrams of the four clusters extend about 1 mag fainter than the horizontal branches of the clusters, allowing easy identification of the horizontal branches. Horizontal branch morphologies change from blue to red with increasing metallicity as expected from Galactic globular clusters.

Surface brightness fluctuation measurements on one cluster in the I band produced a distance modulus to M31 of 24.56 ± 0.12, in statistical agreement with the Cepheid distance modulus of 24.43 (0.77 Mpc) of Freedman & Madore (1990).

The best estimate of the mean brightnesses of RR Lyrae stars, which includes only three clusters, yields $\langle M_V(\mathrm{RR})\rangle = (0.08 \pm 0.13)\,[\mathrm{Fe/H}] + (0.88 \pm 0.21)$, where the zero point assumes a distance modulus to M31 of 24.43. The mild metallicity dependence measured here is slightly lower than slopes of ~ 0.15 (common in the literature), but the values agree within the errors. Slopes of ~ 0.30 or higher appear less likely.

Adopting a metallicity dependence of 0.15 for the three clusters yields a mean zero point of 0.97 ± 0.12 mag, implying that the Cepheid distance scale and the RR Lyrae scale of Carney, Storm, & Jones (1992) are in reasonably good agreement. However, current uncertainties about the WFPC-2 photometric behavior make final conclusions about the photometric zero point less certain. Additional M31 and other Local Group globular cluster observations are needed to calibrate the RR Lyrae stars definitively relative to Cepheids.

---

[1] Based on observations with the NASA/ESA *Hubble Space Telescope,* obtained at the Space Telescope Science Institute, which is operated by the Association of Universities for Research in Astronomy, Inc., (AURA), under NASA Contract NAS 5-26555.

[2] The National Optical Astronomy Observatories are operated by AURA, Inc., under cooperative agreement with the National Science Foundation.

1. Introduction

Distances are fundamental to our physical understanding of the universe. Although careful work over the past several decades has produced accurate distances to most objects of interest to astrophysicists, the *precision* of these distances remains unsatisfactory. The quest for accurate and precise distances is made from many angles, and in this paper we will investigate the RR Lyrae (or horizontal branch [HB]) distance scale. We will present *Hubble Space Telescope* observations of globular clusters in M31 to help improve the accuracy and precision of this distance scale, and we will also compare these results with Cepheid distances.

There are basically two parameters which have been the source of controversy in recent years regarding the RR Lyrae distance scale: the zero point and slope of the absolute magnitudes of RR Lyrae stars as a function of metallicity. Several approaches have been used to determine the parameters in this relation. These include Baade-Wesselink analyses (Carney, Storm, & Jones 1992, hereafter referred to as CSJ; also a good summary of other methods), horizontal branch theory (Lee, Demarque, & Zinn 1990, hereafter referred to as LDZ), the bump in the red giant branch (RGB) luminosity function (Fusi Pecci *et al.* 1990), bolometric magnitude of the tip of the RGB (Da Costa & Armandroff 1990, Ajhar 1992), main-sequence fitting (Buonanno *et al.* 1990), and period-shift analyses (Sandage & Cacciari 1990, Sandage 1993). A short review can also be found in Pritchet (1988). Instead of providing a clear and precise calibration of the RR Lyrae distances, the current literature shows a slope that ranges over a factor of two and a zero point ranging over 0.3 mag.

A method of providing the metallicity dependence of the relation which is cleaner than those listed above would be to observe RR Lyrae stars at the same known distance. We will use a wide of range of metallicities with this method here with the observations of HB stars in M31 globular clusters. In a related approach, Walker (1992) studied RR Lyrae stars in the LMC all at nearly the same metallicity. By adopting a Cepheid distance to the LMC and the CSJ metallicity dependence, he derived a zero point for the absolute magnitudes of metal poor RR Lyrae stars. We will use a similar approach here except that our globular clusters span a large range in metallicity, providing us with an *independent* measurement of the metallicity dependence. In earlier M31 observations, Pritchet & van den Bergh (1987) measured the B magnitude of M31 halo *field* RR Lyrae stars, but unknown metallicities made a metallicity calibration impossible. Note that our observations are merely snapshots of each cluster. Hence, while individual identification of RR Lyrae stars is not possible, we will use the HBs of the clusters to infer the RR Lyrae magnitudes (Sec. 3).

Laying to rest the controversy over the metallicity dependence of RR Lyrae absolute magnitudes would also settle our understanding of the Milky Way globular cluster distance scale, which has immediate implications on the relative ages of the globular clusters. The zero point will also directly affect the absolute ages of globular clusters as determined from theoretical models of stellar evolution. Lastly, it is important that the ultimate RR Lyrae distance scale be consistent with the Cepheid distance scale, which is one of the tools used to determine the distances to M31 and other Local Group (LG) members and ultimately used to calibrate the zero points of many other techniques for measuring extragalactic distances.

In Sec. 2 we present the observations and discuss the photometric methods used, the associated errors, and the calibration to standard photometric systems. In Sec. 3, we use the photometric results discussed in Sec. 2 to analyze the horizontal and red giant branches. We discuss the determination of the horizontal branch level, reddening issues, and surface brightness fluctuation measurements. In Sec. 4, we discuss the implications of these results on the RR Lyrae distance scale and the resulting distance scale of the Galactic globular clusters. Finally, we summarize our results in Sec. 5.

2. Observations and Analysis

2.1. Observations and Initial Reductions

Images of four globular clusters were obtained with the *Hubble Space Telescope* using the Wide Field and Planetary Camera-2 (WFPC-2) on 1994 February 15. Two exposures of 1000 s each were collected in the F555W (V) and the F814W (I) filters. The detector was operating at $-77°$ C in the low-gain setting of 7 e^-. In this paper we focus our discussion on the Planetary Camera (PC) images, which have a pixel size of $0\farcs04554$ and FWHM of about $0\farcs09$ in each image. The Wide Field images and the structural parameters of the clusters are discussed in Grillmair *et al.* (1995).

Each exposure was processed in the usual manner, which we now summarize. First, an analog-to-digital correction was applied to the raw images, and the bias level, determined from a clean area of the overscan region, was subtracted. Next, we subtracted the "superbias" frame and then scaled and subtracted the master "superdark" frame. Since the dark rate is always changing in WFPC-2 (Holtzman *et al.* 1995a), we also subtracted a "local" superdark frame taken within one day of our observations. As a local superdark frame would be dominated by readout noise in pixels with low dark current rates, all pixels whose dark rate was less than about 0.014 $e^- \, s^{-1}$ were set to zero in the local superdark. Although the problems with "hot" pixels was worse at this temperature than at the current WFPC-2 operating temperature of $-88°$ C, applying dark frames in this manner effectively reduced hot pixels to a manageable number. Finally, standard flat fields were used to flatten the data images. High signal-to-noise flat fields were obtained during the thermal-vacuum testing of WFPC-2 to determine high spatial frequency variations in the CCDs' response. The low frequency variations were determined from flat fields taken in orbit.

Once the raw data images were processed, we combined the two 1000 s exposures for each filter while statistically eliminating cosmic rays. All of the exposure pairs were registered without the need to shift any of the images. This left us with 2000 s total exposure time in each filter for each cluster.

We selected clusters for this project that would likely yield well-populated horizontal branches (*i.e.*, relatively bright clusters), cover a wide range of metallicity with relatively small errors, and were not too close to the M31 disk. Table 1 lists the catalogue numbers from Huchra *et al.* (1991) (we will use the second part of these catalogue numbers preceded by "K" to identify each cluster throughout this paper), their spectroscopic [Fe/H] values with errors, our adopted [Fe/H] values, total V magnitudes, and celestial coordinates. The reproduction of the Palomar Observatory Sky Survey E plate (Figure 1) shows the location of these clusters relative to M31, and Table 2 gives the approximate location of each cluster on the sky relative to the center of M31. The first column of Table 2 gives the cluster name, the next two the coordinates in arcmin, the next pair in kpc assuming a distance modulus of 24.43 (770 kpc), the projected radial distance in kpc, and finally the location of the center of each cluster on the PC CCD in pixels. Figures 2–5 show 400 × 400 pixel ($18\farcs2 \times 18\farcs2$) sections of the F555W PC images centered on each cluster.

2.2. Relative Photometry

2.2.1. DoPHOT

The automated photometry program DoPHOT (Schechter *et al.* 1993) performed the point spread function (PSF) fitting to yield relative magnitudes of the stars in the four clusters. Briefly, DoPHOT iteratively models the PSF and fits successively the brightest to faintest objects in the image, removing each one fitted as it proceeds. This process continues until a flux threshold above the background noise is reached. In this case, we used a signal-to-noise threshold of 5 to detect objects. In computing magnitudes of objects, DoPHOT carefully handles sources of error, including noise from the sky and the imperfections of the fit. For these observations, DoPHOT was tuned to match the PSFs as well as the noise characteristics obtained in these observations. Variations in the PSF across the field were small except at the edges of the CCD, where a slight variation is noticeable.

2.2.2. Simulations

We produced simulations to test the performance and accuracy of DoPHOT. The program Tiny Tim (Krist 1995) generated model WFPC-2 PSFs for the F555W and F814W filters which were 512×512 pixels in size and pixelated so that 5×5 pixels corresponded to the size of one PC pixel. For each simulation the model PSF was sampled from different starting positions, covering most of the possible 5×5 subpixelization. Each PSF was then scaled to obtain the desired magnitude before it was placed in the simulated image. Several simulations were produced to check errors and bias of DoPHOT as a function of PSF position on the pixels, density of stars, and background level and noise. DoPHOT analyzed these simulated images in the same manner as the data. A discussion of each of the simulations follows.

The first simulated images consisted of a grid of PSFs ranging in brightness from $V = 21.3$ to 26.8 in steps of 0.5 mag, separated by 40 pixels, and placed on a sky background of about 6 ADU, corresponding to the actual background observed in the four globular clusters. The appropriate read noise (7 e^- per image) and photon noise were added to each pixel.

Figure 6 displays (as circles) the errors in fitted magnitude as a function of fitted V magnitude. A linear fit to these points (down to $V = 25.5$), displayed in Figure 6, shows that any bias introduced by DoPHOT amounts to < 0.01 mag over 5 magnitudes, the range of interest for these data. This test quantifies the reliability of DoPHOT's relative magnitudes for isolated images on a simulated sky background. The squares in Figure 6, which are offset in the abscissa to allow close comparison with DoPHOT, show the errors of manually obtained aperture magnitudes for the brightest bins of stars. These errors result from the read noise and photon noise in the pixels.

There is no systematic offset, but the distribution of errors from the DoPHOT magnitudes is slightly wider and more nearly uniform than the one from aperture magnitudes. The reason is the undersampling of the PSF, which causes slightly larger errors in fitted magnitudes than in aperture magnitudes. We know this because the errors obtained from DoPHOT are closely correlated with the position of the PSF center within a PC pixel. For this reason, the errors in the DoPHOT fitted magnitudes span about ± 3% until the errors become dominated by photon statistics at around $V = 23$. These results emphasize the importance of tuning DoPHOT to match the PSF as closely as possible; furthermore, they suggest that future WFPC-2 observations requiring precision photometry of faint stars in a crowded field should be dithered to improve the PSF sampling in a summed image.

The next set of simulations was performed on the observed clusters and their backgrounds. The goals were to estimate any bias caused by crowding or by the faint, unresolved background and to estimate completeness as a function of magnitude. Simulated stars with $V = 25.56$ and $V - I = 0.39$, corresponding to faint RR Lyrae stars, were placed in the observed images of each cluster. Four hundred, eighty-four stars each separated by 32 pixels were added in a grid to the image in each filter. The grid was then successively shifted by 5 pixels with additional fractional pixel shifts (as described above) to form 9 additional simulations on the same cluster to yield an effective total of 4840 simulated stars in each cluster. DoPHOT was then run on each image of 484 simulated stars in exactly the same manner as on the clusters alone. These simulations aided the selection of a minimum radius for each cluster for computing average HB magnitudes at which incompleteness and bias were negligible.

In the final set of tests, simulated stars with $V = 21.86$ to 26.66 in steps of 0.4 mag and with $V - I = 1.0$ (the approximate color of the lower portion of the giant branch) were placed on grids as above, again totaling 4840 stars in each cluster. In these simulations, only radii outside 128 pixels were considered so that the background level and crowding attributable to the cluster were negligible. The results for K219 are displayed in Figure 7. Each magnitude bin contains ~ 250 stars. Figure 7 shows an apparent bias of about 0.05 mag down to the region of interest, in the sense that the faintest stars were measured to be slightly brighter than the input values. Fortunately, this bias is nearly the same for each cluster so that stars of about the same magnitude (such as HB stars) will all have about the same bias. In any case, the effect is small. Section 4 addresses its implications.

Although completeness below the HB is not a major issue in this paper, we provide a few results that may interest the reader. We consider simulations produced on backgrounds of two extremes of stellar crowding: K219 (least) and K108 (most). (1) In the least crowded simulations, all magnitude bins were more than $\sim 99\%$ complete except for $V = 26.26$ and 26.66, which were 95% and 68% complete, respectively, and the corresponding I-band bins, which were slightly less complete (a few percent). (2) In the most crowded simulations, all magnitude bins were more than $\sim 98\%$ complete except for $V = 25.86, 26.26$, and 26.66, which were 97%, 89%, and 57% complete, respectively, and again the I band was a bit worse. Because measurements discussed in this paper did not require corrections for incompleteness, none were made.

2.2.3. *Comparison with ALLFRAME*

As an additional check, ALLFRAME (Stetson 1994) also processed these cluster data and some of the simulated images. We found similar performance between the programs after proper tuning. We compared CMDs and explored magnitude differences as a function of magnitude. The reported errors were consistent with our findings. We averaged magnitudes of individual stars between the two programs and found that errors from them were correlated as the scatter on the CMDs remained the same. Magnitude offsets between the programs were within the errors of the aperture corrections.

2.2.4. *WFPC-2 CTE Issues*

At its initial warmer operating temperature (and the temperature at which these data were obtained), WFPC-2 had a ~ 10% gradient in photometry across the chip in the sense that objects in high numbered rows were too faint. In addition, the amplitude of the gradient depended on star brightness, being smaller (~ 5%) for the brightest stars and larger (10–15%) for fainter stars. This effect was identified in ω Cen data, which had essentially no background. It was attributed to poor charge transfer at low background levels. Fortunately, the data here have a background level of $\sim 20\ e^-$ in each exposure, which should be more than ample to overcome the earlier problems of WFPC-2 (Trauger 1995).

To verify that no charge transfer efficiency (CTE) problems are detectable in these data, we measured the HB magnitude for K219 using two regions of the CCD. One region consisted of rows above 100 pixels from the center of the cluster; the other of rows 100 pixels below the cluster center. Each region contained about 150 stars. The measured HB levels differed by only 0.02 ± 0.05 mag, based on 14 stars in one region and 6 in the other. This difference was in the opposite sense than expected if caused by CTE problems. Other differences in the color magnitude diagrams (CMDs) of these two regions were attributable to small number statistics. In summary, no CTE problems were detectable in these data although the statistics make it difficult to rule out a small effect. An additional test of CTE problems is presented in Sec. 3.3, where HB magnitudes are compared between two clusters.

2.3. Conversion to Standard System

Standard V and I magnitudes are derived from the WFPC-2 flight system of Holtzman *et al.* (1995b):

$$V = \mathrm{F555W} - 0.052(V-I)_0 + 0.027(V-I)_0^2 + 21.724 + 2.5\log_{10}(1.987) \tag{1}$$

and

$$I = \mathrm{F814W} - 0.063(V-I)_0 + 0.025(V-I)_0^2 + 20.840 + 2.5\log_{10}(1.987) + 0.05, \tag{2}$$

where $(V - I)_0$ is determined iteratively for each star after applying the appropriate extinction correction to the observed magnitudes for each cluster. There is further discussion of extinction corrections in Sec. 3.2. Equation 2 has had 0.05 added to it to reflect the higher quantum efficiency (QE) of the CCD at earlier high temperature (see Holtzman *et al.*); as a result, the zero point in I is less certain than in V, where the QE is expected to be constant in this temperature range.

An additional concern is the exact zero point. Holtzman *et al.* mention that several observers have reported observations of the same field with different exposure times yielding zero point differences of up to 0.05 mag. Although there is currently no physical explanation for this effect even if true, the reader should note that the magnitudes reported in this paper are all from long exposures and may therefore be too bright by ~ 0.05 mag relative to the ω Cen zero points. This phenomenon remains under investigation.

Holtzman *et al.* note that stars outside the range $-0.3 < (V-I)_0 < 1.5$ may not be accurately transformed using Equations 1 and 2; however, this generally does not significantly affect the science presented in this paper. Holtzman *et al.* also report the errors in these transformations to be < 2%.

An aperture correction was applied to DoPHOT magnitudes to match the $0\farcs5$ radius aperture photometry used by Holtzman *et al.* For each filter and for each cluster, about 10 to 12 of the brightest, most isolated stars were examined. The differences between $0\farcs5$ aperture magnitudes and the magnitude fitted by DoPHOT for each star were averaged, and the resulting aperture correction was then applied to all of the stars for the particular filter and cluster. In V the rms scatter in the aperture corrections ranged from 0.04 to 0.10 mag, and in I the scatter ranged from 0.04 to 0.06 mag. The net effect is an additional ~ 0.01 to 0.03 mag rms error added in quadrature to the end zero point.

2.4. The Color-Magnitude Diagrams

Figures 8–11 display the CMDs of the four clusters. Only stars outside a radius of 64 pixels ($2\farcs91$) and inside a radius of 256 pixels ($11\farcs66$) from the cluster centers are shown (except that K219's outer radius extends to 400 pixels, or $18\farcs22$). Inside 64 pixels radius, crowding begins to introduce substantial errors and confusion, as we shall see later. The CMDs with V as the ordinate clearly show the horizontal branches of the two metal poor clusters K105 and K219 while red clumps are visible in the metal rich clusters K58 and K108 (although the red clump in K108 is heavily contaminated by the M31 field). The CMDs with I ordinates show the giant branches better because the giant branch is stretched over a greater magnitude range. Note that the HST CMDs presented here are similar to ground-based CMDs of the centers of Milky Way globular clusters.

Because of the completeness limits of these data, the morphology of the HBs of these clusters is potentially misleading. These CMDs do not show a "blue tail" on any of the HBs, but the I-band measurements are not deep enough to reveal one if it exists (*cf.* Sec. 3.3).

3. Results

3.1. Horizontal Branches

To compare HB stars of M31 globular clusters with those of the Milky Way and its clusters, we must first identify the HB stars and separate them as effectively as possible from any contaminating stellar population. Figures 12–15 display the CMDs of each cluster in six different annuli centered on each cluster. These figures aid identification of cluster stars, which comprise the horizontal and giant branches. The innermost annuli ($r < 32$ pixels [$1\farcs46$]) are densely populated with stars, and the resulting blending of stars produces poorly defined, noisy CMDs. The next annulus ($32 < r < 64$ [$2\farcs91$]) shows a marked improvement for each cluster, but completeness and noise from the blending of stars are still unacceptable. Outside $r = 64$, crowding is no longer a major contributor to the errors, but the largest annuli are dominated by contaminating stellar populations. The most clearly defined, least contaminated CMDs occur in the range $64 < r < 256$ ($11\farcs66$) for K58 and K105. This range is easily extended to $64 < r < 400$ ($18\farcs22$) for K219, which has very little contamination. The analysis of the giant branches of these clusters described in Sec. 3.2 was confined to these radial ranges.

The best radial range to sample the image for HB magnitudes was determined by combining knowledge gained from the simulations discussed in Sec. 2.2.2 with the observations. We only selected a range in radius in which the observed mean HB magnitudes within each cluster did not vary with radius. This gives us confidence that any radial bias is negligible without sole reliance on simulations and that we understand the completeness in our selected radial interval. The best radial ranges in pixels were found to be 100 to 128, 80 to 256, and 128 to 400 for K58, K105, and K219, respectively. The discussion of HB magnitudes that follows includes only those stars in these radial intervals. For K108, which also has the least populated giant branch, contamination is the worst, and clean measurements of its horizontal branch are difficult. However, the contaminating population itself provides excellent statistics on the local M31 field, which consists of a mixture of halo and outer disk stars roughly along the minor axis. Stars beyond 256 pixels in radius are referred to as the "K108 Field." The field near K58 ($r > 256$) provides yet another sample of stars with a different mix of halo and outer disk, a little further out but roughly in the same direction. Because the K105 and K219 Fields have comparatively fewer stars on the PC images, they are not discussed in this paper.

Since the HBs of metal poor and metal rich clusters have different morphologies, the technique used to determine the mean RR Lyrae brightness is different for these clusters. The first part of this discussion is limited to the metal poor clusters K105 and K219, which have blue branches. For these clusters we identify the likely population of RR Lyrae stars by color and simply take their mean brightness. For the metal poor clusters the RR Lyrae stars are found in the interval $0.3 < (V-I)_0 < 0.8$ based on the CMDs of Ajhar (1992). Unfortunately, this entire interval cannot be used since errors in the RGB at the level of the HB may contaminate the red end of the HB sample. Instead, the interval is limited to $0.3 < (V-I)_0 < 0.6$, where contamination from the RGB is negligible. The HB sample is further limited to ±0.7 mag from the mean to minimize contributions from contaminating populations. The magnitudes were corrected for extinction (discussed below) before obtaining the sample in each case. Figures 9 and 11 show that incompleteness is negligible in this interval. The rms's in V were 0.14 mag and 0.25 mag for the HB samples of K105 and K219, and the samples consisted of 8 and 22 stars, respectively. The mean observed values were 25.50 ± 0.05 mag for K105 and 25.27 ± 0.05 mag for K219.

For the metal rich cluster K58, the luminosity function (LF) (Figure 16) clearly reveals the HB, which is a "red clump" similar to that found in 47 Tuc. First, the LF of the M31 background field ($r > 256$) is measured and smoothed, and the number counts are normalized to the same sky area as the inner cluster sample. The resulting background LF, displayed in Figure 16, is then subtracted from the K58 LF.

The red clump peak of K58 is taken as the mean level of the HB (see below). Because the LF contains both RGB and HB stars, an estimate of the number of RGB stars is removed from the LF before measuring the peak. A power law (a linear fit in the displayed logarithmic coordinates) is a good fit to the RGB LF above and below the HB clump. After subtracting this function, the HB level is determined by fitting a quadratic to the red clump peak (in logarithmic coordinates). Fortunately, the relatively large ratio of HB stars to RGB stars means that the resulting peak position is only mildly sensitive to the choice of power law slopes, such that a factor of 2 increase in slope results in a shift of only ~ 0.02 mag in the position of the peak. The same procedure was used on both the K58 and K108 Field regions. We found the peak values to be 25.47 mag, 25.45 mag, and 25.55 mag for K58, K58 Field, and K108 Field, respectively. The reader should note that because the brightness of the red clump is not necessarily the same as RR Lyrae stars of the same metallicity, an adjustment will have to made to the values determined here for metal rich populations. This adjustment is discussed in Sec. 3.3.

3.2. Metallicity and Reddening from Giant Branches

We next need to adopt accurate metallicities and reddenings for each cluster in order to interpret the HB magnitudes properly. The procedure here is first to determine the metallicities and then the reddenings from the shape and color of the giant branches. These determinations will provide an independent check on the spectroscopic metallicity measurements and the Galactic H I reddening measurements of Burstein & Heiles (1982). The clusters are so far from the disk of M31 that reddening within it should be small.

The spectroscopy of Huchra *et al.* (1991) provide reasonable estimates of the metallicities of these clusters, but the present CMDs provide an opportunity to verify or improve those measurements. We will estimate metallicities by using the standard giant branches of Da Costa & Armandroff (1990), who give the shapes of six globular cluster giant branches in V and I with [Fe/H] ranging from −0.71 to −2.17. The spectroscopic metallicities guide the comparison with the standard giant branches. First, we trace the ridge line of the giant branch for each cluster. Then, allowing the standard giant branches with metallicity similar to the cluster freedom to float in $(V-I)_0$ and I (no rotations), we shift them to match the cluster best. The shapes of the giant branches near the tops of the most metal poor clusters are similar; thus, distinguishing metallicities among these is the most difficult. The relative ease of uniquely matching giant branches increases as the metallicity increases. Although simple, this technique is a useful check on cluster metallicities to the accuracy and precision needed for this project.

The left panel of Figure 17 repeats the CMD of the most metal poor cluster K219 with the ridge line superposed. The right panel displays the K219 giant branch with those of M15 and NGC 6397, whose [Fe/H] values are −2.17 and −1.91, respectively. The difficulty of distinguishing between these two metallicities is apparent and results from the relative straightness of the standard giant branches, the small number of tip stars in the cluster, as well as the increase in the observed giant branch width as the photometric errors increase at fainter magnitudes. Even with this difficulty, [Fe/H] is likely to be somewhere between these two standards at -2.04 ± 0.22, which is consistent with the spectroscopic value listed in Table 1. We adopt the metallicity based on the CMDs.

Figure 18 shows a similar CMD for K105. The right panel displays the K105 giant branch along with those of NGC 6397 and NGC 6752, whose metallicities are −1.91 and −1.54, respectively. Here the match to NGC 6752 is excellent, while it is obvious that NGC 6397 is more metal poor than K105. This verifies the spectroscopic metallicity of -1.49 ± 0.17, which we now adopt. As the K105 giant branch is not as well populated as the one in K219, it is possible that the brightest stars are "missing" from the CMD, making the NGC 6752 giant branch tip appear brighter.

The CMD for K58 appears in Figure 19. The choice of giant branch ridge line is guided by the inner annuli in Figure 12, where the true curved shape of the cluster locus is evident. The right panel of Figure 19 compares K58 with the giant branch of 47 Tuc—whose metallicity is −0.71, the most metal rich cluster of the Da Costa & Armandroff giant branches. One can only conclude from this comparison that K58 is indeed more metal rich than 47 Tuc, in agreement with the spectroscopic value of -0.57 ± 0.15. A more precise value than this is difficult because the color terms for stars redder than $(V-I)_0 = 1.5$ are uncertain and because no precise standards exist for CMD comparisons.

Finally, Figure 20 shows the CMD of K108. This CMD comes from the annulus defined by $64 < r < 128$ pixels. In this annulus the background contamination is ~ 27 %, based on the flux from the area $r > 400$. The giant branch trace shown in the left panel is compared in the right panel with 47 Tuc ([Fe/H] = −0.71) and NGC 1851 ([Fe/H]= −1.29). The RGB of K108 is a very close match to 47 Tuc except at the very tip (where our ridge line is uncertain because of the poorly populated RGB), and this suggests that K108 may be slightly more metal poor than 47 Tuc. However, we remind the reader that the conversion from WFPC-2 magnitudes to standard magnitudes is uncertain for stars redder than $(V-I)_0 = 1.5$. The spectroscopic value has K108 at -0.94 ± 0.27, which agrees fairly well with our determination of the giant branch. We choose to adopt −0.80 for K108, based on its closer agreement with the RGB of 47 Tuc.

We use isochrones for the natural WFPC-2 filters calculated by Worthey (1995) to estimate the metallicities of the K58 and K108 Fields. Figures 21 and 22 show various model RGBs superimposed on the observed data. We have assumed a distance modulus of 24.43 mag and reddenings from Table 3. For a young (2 to 5 Gyr) population, these models suggest that [Fe/H] $\approx -0.2 \pm 0.2$ for the K58 Field and [Fe/H] $\approx -0.15 \pm 0.2$ for the K108 Field. For a 10 Gyr population, the models suggest that [Fe/H] $\approx -0.4 \pm 0.1$ for the K58 Field and [Fe/H] $\approx -0.35 \pm 0.1$ for the K108 Field. (For a 15 Gyr population, [Fe/H] would be closer to about -0.5.) We will adopt -0.3 ± 0.2 and -0.25 ± 0.2 for the respective field populations. These are reasonable estimates if the M31 field is anything like that of the Milky Way.

The metallicity determinations from above aid the determinations of reddening corrections to apply to each cluster. Sarajedini (1994) provides a method to determine [Fe/H] and E_{V-I} simultaneously from the giant branch. This method is based on the standard giant branches of Da Costa & Armandroff and is tied to their metallicity and reddening scales but is independent of the RR Lyrae distance scale. Because higher precision photometry than the current data provide are really needed for this method and because we have spectroscopic measurements of [Fe/H] already, we employ this method only to determine reddening, keeping metallicity fixed. Equation (3) of Sarajedini gives

$$E_{V-I} = (V-I)_g - 0.1034[\mathrm{Fe/H}] - 1.100, \tag{3}$$

where $(V-I)_g$ is the color of the RGB as measured at the level of the HB. One can readily see that our errors in [Fe/H] are only a small contribution to the error in E_{V-I}. Also, Figures 17–19 reveal that $(V-I)_g$ is nearly constant near the level of the HB, and this results in errors in E_{V-I} that are dominated by our systematic photometric errors.

The reddening law used by Da Costa & Armandroff has

$$A_V : A_I : E_{B-V} = 3.200 : 1.858 : 1.000, \tag{4}$$

which is similar to what Holtzman *et al.* (1995b) give for the WFPC-2 filters

$$A_{\mathrm{F555W}} : A_{\mathrm{F814W}} : E_{B-V} = 3.27 : 1.91 : 1.00, \tag{5}$$

from an average of extinction corrections for O6 and K5 spectra. We adopt equation 4. The resultant values of E_{B-V} and their errors are compared to values extracted from the maps of Burstein & Heiles (1982) in Table 3. The agreement is within the errors for all clusters. We choose to adopt the values from Burstein & Heiles because (1) those reddening values are not subject to the same systematic errors *relative* to each other as the photometric values and (2) the Burstein & Heiles values also provide a measurement for K108 and the K108 Field (we do not have photometric estimates for these because the K108 red clump is too heavily contaminated by M31 stars and the metallicity of the K108 Field is not precisely known).

Figure 23 shows the giant branches of all four clusters after extinction corrections are applied. The increase in curvature of the RGB as metallicity increases is evident, as is the constancy of the RGB tip magnitude, excepting K105, which is perhaps more distant or has an unpopulated tip.

3.3. Horizontal Branch and RR Lyrae Magnitudes

Table 3 lists the observed HB magnitudes (fourth column) and their dereddened values (fifth column). The errors listed in the fifth column include contributions from aperture corrections, uncertainties in E_{B-V}, uncertainty in the reddening law adopted, and uncertainty in the measured HB magnitude. The final column lists the RR Lyrae magnitude inferred from the HB magnitude. For the metal poor clusters K105 and K219, these values are the same. Adjustments made to the HB magnitudes of the metal rich populations are discussed next.

Because HB magnitudes of metal rich populations (which generally contain no RR Lyrae stars because they are most likely too young) are determined from red clumps, one must infer the corresponding magnitude of RR Lyrae stars for these populations before comparing to the HBs (RR Lyrae stars) of metal poor clusters. According to theory, the V magnitude difference ΔV between RR Lyrae and red clump stars varies in large part with [Fe/H] and age. Model HBs can predict ΔV for a grid of [Fe/H] and age but cannot *a priori* predict an expectation value for ΔV for a given globular cluster—precisely the value needed here—without detailed knowledge of the cluster's chemistry and age. If red clump and RR Lyrae stars existed simultaneously in many Galactic GCs, one could find the expectation of ΔV observationally without resorting to theory. Unfortunately, such clusters do not exist (except 47 Tuc, which has one RR Lyrae star). As a result, we will determine the expectation of ΔV by averaging theoretical ΔV's for several observed Galactic GCs. We averaged ΔV for the metal rich clusters from Sarajedini *et al.* (1995). Specifically, these were NGC 6624, NGC 6637, 47 Tuc, Pal 12, and Lindsay 1, having the respective metallicities of $-0.51, -0.58, -0.71, -1.06$, and -1.10. Sarajedini *et al.* (1995) predict M_V of the HB red clump peak from the observed [Fe/H] and d_{B-V}, the difference in $B-V$ color between the peak of the HB red clump and the ridge line of the RGB at the V magnitude level of the HB, by using theoretical HB models (see LDZ and Lee *et al.* 1994). We then take the difference between the predicted M_V's of the HB red clump peaks and M_V(RR) predicted for RR Lyrae stars in clusters of the same metallicity using the same models, specifically $M_V(\mathrm{RR}) = 0.17\,[\mathrm{Fe/H}] + 0.79$ (Lee 1990). From this we find the average difference ΔV among the five clusters to be 0.077 mag, with an rms of 0.035 mag, in the sense that the red clump is brighter than the RR Lyrae stars. This result gives us a reasonable estimate of the expectation of ΔV, based on one set of theoretical HB models and several observed clusters. It also agrees with the estimate of ΔV used by Fullton *et al.* (1995) of 0.10 ± 0.05 mag.

The biggest surprise of these results is the difference of 0.23 ± 0.11 mag between the two metal poor clusters K105 and K219. This is $\sim 2\ \sigma$, but additional checking is warranted. First, we return to the question of CTE because these two clusters were observed on different areas of the chip (see Table 2), K219 (and the other clusters) centered slightly below the center rows of the CCD and K105 above. Because K105 has the faintest HB and it is located among the highest rows, a problem with CTE could account for a fair fraction of this difference ($\sim$ 0.05–0.10 mag). As a check for this problem, we examined HB stars of both clusters from a common region of rows on the CCD. Specifically, we selected 12 stars in K219 and 7 stars in K105 which were isolated and had $400 < y < 580$ pixels. Aperture photometry with a radius of 5 pixels (to minimize photometric errors) yielded a difference in mean HB magnitude of 0.19 mag between the two clusters in the above sense while DoPHOT for the same stars yielded 0.17 mag, in fair (but not perfect) agreement. While it is possible that potential CTE problems may account for some of the difference in magnitude between these two clusters, it is probable that a genuine difference remains in the data.

Another possibility, though unlikely, is that the He abundance Y differs between the two clusters. A larger value of Y in K219 would be in the right sense. We applied the R' method of Buzzoni *et al.* (1983) to determine if useful limits could be placed on ΔY between the two clusters. Using

$$Y = 0.43 \log_{10} R' + 0.210, \tag{6}$$

where $R' = N_{\rm HB}/(N_{\rm RGB} + N_{\rm AGB})$, we found that $Y > 0.11$ for K219 and $Y > 0.06$ for K105. Although the limit on Y in K219 is indeed larger, neither value is meaningful owing to undetected HB stars below the photometric threshold. This may be seen as follows: For the metal poor MW clusters of Buzzoni *et al.* (47 Tuc excluded), the mean R' is 1.15, implying a mean $Y = 0.23$. Assuming that Y in M31 is similar to that in the MW yields the following results. For $r > 64$ pixels, K219 has 179 HB stars and 300 GB stars, implying that there are approximately 150 to 180 HB stars undetected. For K105 in the region $64 < r < 256$, there are ~ 48 HB and ~ 109 GB stars net of background, implying that approximately 65 to 85 HB stars are undetected. If these assumptions are correct, it is likely that both clusters exhibit blue tails in their HBs and that deeper exposures would reveal the full morphology of their HBs.

3.4. Fluctuation Measurements

The cluster K219 is large enough and has low enough contamination to yield a useful measurement of its surface brightness fluctuations (SBF). SBF measurements provide a separate distance estimate to K219, which we will compare to the Cepheid distance to M31. Following Ajhar & Tonry (1994), the apparent fluctuation magnitude $\overline{m}$ is determined by converting the following mean flux to a magnitude:

$$\overline{f} = \frac{\sum f_i^2}{\langle f \rangle}, \tag{7}$$

where f_i are individual stellar fluxes in some region of the cluster and $\langle f \rangle$ is the total cluster flux over the same region. Ajhar & Tonry found that $\overline{M_I} = -2.02 \pm 0.04$ (independent of metallicity) among Galactic globular clusters, based on the distance scale of CSJ.

For this measurement, we shifted the region considered inward to minimize the effect of small number statistics on the measurements. The slightly larger scatter of the RGB in the region $32 < r < 64$ (*cf.* Figure 15) is more than offset by a 25% decrease in the random scatter of the total measurement. The total V magnitude in the region $32 < r < 256$ is 15.65, which gives

$M_{V,\mathrm{tot}} \sim -8.8$ for an M31 distance modulus of 24.43 (Freedman & Madore 1990). In the same region $\overline{m}_I = 22.65 \pm 0.09$, $\overline{m}_V = 24.25 \pm 0.07$, and $(\overline{V} - \overline{I})_{\mathrm{app}} = 1.61 \pm 0.03$. Corrected for reddening, these become $\overline{I} = 22.54$, $\overline{V} = 24.06$, and $\overline{V} - \overline{I} = 1.53$. The fluctuation color $\overline{V} - \overline{I}$ has the smallest error because the random errors of $\overline{V}$ and $\overline{I}$ are correlated.

We next compare these results with those of other clusters of this metallicity. Table 4 lists three clusters from Ajhar & Tonry. The integrated $(V-I)_0$ colors are similar to that of K219, which is 0.83 ± 0.013 in the region $r < 256$. K219's $\overline{V} - \overline{I}$ also compares closely. As mentioned above, $\overline{M}_I = -2.02$, while Table 4 suggests that $\overline{M}_V$, which varies with metallicity, is ~ -0.54. These yield distance moduli to K219 (with errors that are highly correlated) of 24.56 and 24.60 mag, respectively, based on the CSJ distance scale. The formal 1σ errors here are ~ 0.1 mag; including uncertainties in reddening and photometric zero points would increase this to ~ 0.12 mag, putting this measurement within about 1σ of the Freedman & Madore (1990) value of 24.43, which has similar errors.

4. Discussion

Having determined RR Lyrae magnitudes for the clusters and M31 fields in Sec. 3.3, we can now consider the calibration of the RR Lyrae distance scale. For simplicity we adopt the M31 Cepheid distance modulus of Freedman & Madore (1990) of 24.43, corresponding to 0.77 Mpc. Note that some authors prefer a closer distance, such as 24.3 of Hodge (1992). While this choice has no effect on the following discussion of the metallicity dependence of RR Lyrae magnitudes, the choice is important for comparison with RR Lyrae zero point calibrations.

In Section 3, measurement errors were tracked at each step in the reductions, and metallicities and reddenings were verified as carefully as possible. The only other known, potentially significant uncertainty is the individual distance to each cluster. Although Section 3.4 contains additional distance information from which we can draw, this method ultimately relies on the clusters all being roughly at the M31 distance. Having a large sample of cluster observations will eventually reduce the error in the final results. For now, each RR Lyrae magnitude listed in the last column of Table 3 was converted to an absolute magnitude using a distance modulus of 24.43, and a linear metallicity dependence was fitted and found to be

$$\langle M_V(\mathrm{RR})\rangle = (0.04 \pm 0.07)\,[\mathrm{Fe/H}] + (0.80 \pm 0.09). \tag{8}$$

For each cluster a generous 0.1 mag error (at M31 this corresponds to about ±35 kpc in distance) was added in quadrature to those listed in Table 3 to allow for possible scatter in the distances to individual clusters. The errors in [Fe/H] are from Table 1 while the metallicity errors for the HBs of the K58 and K108 Fields were adopted to be ±0.2 dex (see Sec. 3.2). Figure 24 displays the RR Lyrae magnitudes as a function of metallicity. The clusters are plotted with filled circles while the field populations are plotted with open circles. Any metallicity dependence has essentially been washed out by the errors (including the uncertainty in distances to the clusters) and perhaps by some other parameter or parameters affecting the RR Lyrae magnitudes. In the context of earlier determinations of the metallicity dependence, this result is statistically consistent with measured slopes of $\sim$ 0.15; however, slopes significantly larger than that are less likely (*e.g.*, Sandage 1993, who reports 0.30).

These results raise some interesting questions. The unusually weak metallicity dependence may suggest that other parameters (such as age and Helium abundance) are indeed affecting the RR Lyrae magnitudes. This idea was recently suggested by van den Bergh (1995) to explain the apparent discrepancy between the RR Lyrae and Cepheid distances to the LMC ($\sim$ 0.3 mag). While the difference here is not sufficient to demand new parameters, a bit of a puzzle remains. The three metal rich populations (namely K58, K58 Field, and K108 Field) yield $V_0(\mathrm{RR}) \sim 25.2$ while the the metal poor clusters (K105 and K219) yield $V_0(\mathrm{RR})$ of ~ 25.3 and ~ 25.1.

One obvious potential problem lies with the metal rich populations. The magnitude difference between RR Lyrae stars and HB red clump stars is not exactly known. We have already adjusted the red clump magnitudes fainter by 0.077 mag to infer the RR Lyrae magnitudes (see Sec. 3.3).

While this seems appropriate for K58, it may not at all be proper to use for the K58 and K108 Fields, owing to their possible younger age. Using only K58, K105, and K219, the best fitting metallicity dependence is

$$\langle M_V(\mathrm{RR})\rangle = (0.08 \pm 0.13)\,[\mathrm{Fe/H}] + (0.88 \pm 0.21). \tag{9}$$

These parameters, although more poorly constrained, are perhaps the safest estimates from this limited data set because the selection of objects is confined to clusters which are similar to those found in the Milky Way. Equation 9 is plotted on Figure 24.

Further theoretical work is really needed to interpret these data—as well as more CMDs of other LG GCs. What is the magnitude difference between the red clump and the RR Lyrae stars for young, metal rich populations such as the K58 and K108 Fields? What parameters besides [Fe/H] and Y have a significant effect on the brightness of RR Lyrae stars and red clumps, and exactly how is the brightness a function of these parameters? For example, if the appropriate magnitudes to use for the K58 and K108 Fields are really 0.1 mag fainter (this is approximately what one would get by extrapolating the theoretical curves shown in Figure 5 of Sarajedini *et al.* [1995]), then equation 8 would have had a slope of 0.10 ± 0.08 and a zero point of 0.90 ± 0.09, which is similar to equation 9, but with less scatter.

The results presented here support a weak metallicity dependence of M_V(RR) as argued by CSJ and others (*e.g.*, LDZ) over that preferred by Sandage (1993); however, equation 9 does not constrain the slope well enough to eliminate a fairly strong metallicity dependence. The ultimate precision in determining the metallicity dependence of M_V(RR) will be had when many CMDs of M31 and other LG globular clusters have been studied in detail with HST over the next several years. Ultimately, all of these observations taken together should provide a good calibration of [Fe/H] and $\langle M_V(\mathrm{RR})\rangle$.

The zero point of the M_V(RR) relation (equation 9) is another important topic. Using the Baade-Wesselink technique, CSJ found the zero point to be 1.01 and the metallicity slope to be 0.15. While adopting the same metallicity dependence, Walker (1992) argued for a zero point of 0.73, based on RR Lyrae stars in the LMC and the LMC Cepheid distance. Assuming the same metallicity dependence of 0.15, one finds the mean zero point from the three cluster HBs to be 0.97 ± 0.12 mag (all five HBs yield 0.91 ± 0.13 mag). Although this is in good agreement with CSJ, there are several caveats to consider: (1) The photometric zero point used for these data is uncertain and may be too bright by ~ 0.05 mag (see Sec. 2.3). In addition, these data were taken at the higher WFPC-2 operating temperature, and we have assumed that the F555W QE was not significantly affected by the change of CCD temperature. (2) The simulations suggest that magnitudes at the level of the HB may be systematically too bright by ~ 0.05 mag (see Sec. 2.2.2). While this does *not* affect the comparison of HBs among the clusters for the metallicity dependence, it would make the *zero point* of the RR Lyrae calibration too bright. (3) A slope of 0.15 is *not* the best fit to our M31 data. (4) Assuming a slope 0.15 and using only the three most metal *rich* populations yields an average zero point of 0.82 ± 0.04 mag, which slightly favors Walker. With these caveats in mind, one can conclude nothing definite yet about the zero point with this data set, although it appears that the CSJ zero point is slightly favored by assuming a metallicity dependence of 0.15. One needs to learn more about the photometric zero point behavior of WFPC-2 before drawing further conclusions. Uncovering and resolving potential problems would help furnish the missing pieces of the LG distance ladder puzzle.

5. Summary

Hubble Space Telescope observations of four globular clusters in M31 yielded deep images in V and I. Careful application of the automated photometry program DoPHOT produced color magnitude diagrams extending about 1 mag fainter than the horizontal branches of the clusters. Simulations provided a check on the accuracy of DoPHOT photometry. The CMDs were used to determine accurate metallicities and reddenings for each cluster. The first step of this process was to determine the metallicity from the shape of the red giant branch. The ridge line of each cluster's giant branch was compared to the standard giant branches of Da Costa & Armandroff (1990), confirming the spectroscopic metallicities of Huchra *et al.* (1991) in each case. Two methods were applied to derive reddenings. First, the location of each cluster on the H I map of Burstein & Heiles (1982) gave a first estimate of reddening. These were checked using a modification to the method of Sarajedini (1994), based on giant branch color and assumed [Fe/H]. The two methods agreed within the errors, and the Burstein & Heiles values were adopted.

The CMDs of three of the four clusters allowed easy identification of the horizontal branches, which were used in the analysis. Because the HB of K108 was heavily contaminated by the M31 field, it was omitted from the analysis. Similar to Galactic globular clusters, the morphologies of the horizontal branches change from blue to red with increasing metallicity. For the metal poor clusters the mean magnitude of HB stars in the instability strip defined the level of the HB. For the metal rich clusters the position of the peak in the V luminosity function at the red clump defined the level of the HB, which was subsequently adjusted to the corresponding RR Lyrae star brightness. In addition, two of the clusters had significant contamination from the M31 field population. The red clumps of the outer parts of these images, dominated by the M31 field, defined the level of the HB for the field star population at two locations in M31.

SBF measurements on K219 in the I band produced a distance modulus to M31 of 24.56 ± 0.12 in statistical agreement with the Cepheid distance modulus of 24.43 (Freedman & Madore 1990).

The horizontal branch levels of these clusters plus the two background fields produced a best fitting dependence of RR Lyrae magnitude on [Fe/H] such that $\langle M_V(\mathrm{RR})\rangle = (0.04 \pm 0.07)\,[\mathrm{Fe/H}] + (0.80 \pm 0.09)$, where the zero point assumes the Cepheid distance modulus to M31 of 24.43 mag (0.77 Mpc). A safer estimate includes only the three clusters and yields $\langle M_V(\mathrm{RR})\rangle = (0.08 \pm 0.13)\,[\mathrm{Fe/H}] + (0.88 \pm 0.21)$. The mild metallicity dependence in both fits is lower than but is in statistical agreement with slopes of ~ 0.15 (*e.g.*, CSJ and LDZ), while slopes ~ 0.30 (Sandage 1993) or higher (Sandage & Cacciari 1990) appear less likely. The weak metallicity dependence found here may suggest that other parameters are affecting the RR Lyrae magnitudes, as recently suggested by van den Bergh (1995). However, a final resolution will require more clusters and further theoretical work to understand fully how RR Lyrae magnitudes are affected by parameters other than [Fe/H] and they relate to the HB red clump.

Yet a third zero point of 0.97 ± 0.12 can be derived using just the three clusters and assuming that the metallicity dependence is 0.15. Like all of our zero points, this result relies on the assumed

Cepheid distance modulus to M31 of 24.43 and is therefore subject to revision. In addition, current uncertainties concerning the WFPC-2 photometric zero points affect all of the photometry at the level of ~ 0.05 mag. Nevertheless, this number agrees slightly better with the RR Lyrae zero point of 1.01 by CSJ, as opposed to the LMC zero point of 0.73 by Walker (1992). While these early results are encouraging, additional M31 and LG CMDs are needed to calibrate RR Lyrae absolute magnitudes fully.

We would like to thank A. Sarajedini and T. Armandroff for helpful discussions. This research was conducted by the WFPC Investigation Definition Team, supported in part by NASA Grant No. NAS5–1661.

Table 1. M31 Globular Cluster Sample

Name	$[Fe/H]_{spec.}$	$[Fe/H]_{adopted}$	V_{tot}	α (1950)	δ (1950)
006-58	-0.57 ± 0.15	-0.57 ± 0.15	15.80	$00^h\,37^m\,43\overset{s}{.}1$	$+41^\circ\,11'\,00''$
343-105	-1.49 ± 0.17	-1.49 ± 0.17	16.35	$00^h\,38^m\,58\overset{s}{.}6$	$+39^\circ\,55'\,56''$
045-108	-0.94 ± 0.27	-0.80 ± 0.27	15.80	$00^h\,38^m\,59\overset{s}{.}2$	$+41^\circ\,17'\,54''$ [a]
358-219	-1.83 ± 0.22	-2.04 ± 0.22	15.10	$00^h\,40^m\,34\overset{s}{.}2$	$+39^\circ\,32'\,48''$

[a] This coordinate is incorrect in Huchra *et al.* (1991).

Table 2. Cluster Locations

Cluster	x (′)	y (′)	x (kpc)	y (kpc)	r (kpc)	x (pixels)	y (pixels)
K58	+25	+11	+5.6	+2.5	6.1	455	276
K105	+11	−64	+2.5	−14	14	459	605
K108	+11	+18	+2.5	+4.0	4.7	461	333
K219	−6	−88	−1.3	−20	20	447	299

Table 3. Horizontal Branch Magnitudes

Name	$E_{B-V,\mathrm{S}}$	$E_{B-V,\mathrm{B\&H}}$	V(HB)	V_0(HB)	V_0(RR)
K58	0.089 ± 0.02	0.11 ± 0.03	25.47	25.12 ± 0.11	25.20
K58 Field	0.089 ± 0.02	0.11 ± 0.03	25.45	25.10 ± 0.11	25.18
K105	0.054 ± 0.02	0.06 ± 0.01	25.50	25.31 ± 0.08	25.31
K108	…	0.12 ± 0.03	…	…	…
K108 Field	…	0.12 ± 0.03	25.55	25.17 ± 0.11	25.24
K219	0.076 ± 0.02	$< 0.06 \pm 0.01$	25.27	25.08 ± 0.07	25.08

Table 4. Milky Way Cluster Fluctuation Magnitudes

NGC	Messier	[Fe/H]	$(V-I)_0$	$\overline{M}_V$	$\overline{M}_I$	$\overline{V}-\overline{I}$
2419	···	−2.10	0.85 ± 0.07	−0.52 ± 0.09	−2.04 ± 0.12	1.52 ± 0.08
6341	92	−2.24	0.86 ± 0.04	−0.58 ± 0.17	−2.17 ± 0.20	1.59 ± 0.07
7078	15	−2.15	0.83 ± 0.07	−0.52 ± 0.11	−2.00 ± 0.13	1.48 ± 0.08

REFERENCES

Ajhar, E. A. 1992, Ph.D. thesis, Massachusetts Inst. of Technol.

Ajhar, E. A., & Tonry, J. L. 1994, ApJ, 429, 557

Buonanno, R., Cacciari, C., Corsi, C. E., & Fusi Pecci, F. 1990, A&A, 230, 315

Burstein, D., & Heiles, C. 1982, AJ, 87, 1165

Buzzoni, A., Fusi Pecci, F., Buonanno, R., Corsi, C. E. 1983, A&A, 128, 94

Carney, B. W., Storm, J., & Jones, R. V. 1992, ApJ, 386, 663 (CSJ)

Da Costa, G. S., & Armandroff, T. E. 1990, AJ, 100, 162

Freedman, W. F., & Madore, B. F. 1990, ApJ, 365, 186

Fullton, L. K., et al. 1995, AJ, 110, 652

Fusi Pecci, F., Ferraro, F. R., Crocker, D. A., Rood, R. T., & Buonanno, R. 1990, A&A, 238, 95

Hodge, P. 1992, The Andromeda Galaxy (Boston: Kluwer)

Holtzman, J. A., et al. 1995a, PASP, 107, 156

Holtzman, J. A., et al. 1995b, preprint

Huchra, J. P., Brodie, J. P., & Kent, S. M. 1991, ApJ, 370, 495

Grillmair, C. J. et al. 1995, in preparation

Krist, J. 1995, in Astronomical Data Analysis Software and Systems IV, e. R. A. Shaw, H. E. Payne, & J. J. E. Hayes (Provo, UT: BYU Print Services), 349

Lee, Y.-W. 1990, ApJ, 363, 159

Lee, Y.-W., Demarque, P., & Zinn, R. 1990, ApJ, 350, 155 (LDZ)

Lee, Y.-W., Demarque, P., & Zinn, R. 1994, ApJ, 423, 248

Pritchet, C. J. 1988, in The Extragalactic Distance Scale, e. S. van den Bergh & C. J. Pritchet (Provo, Utah: BYU Print Services), 59

Pritchet, C. J., & van den Bergh, S. 1987, ApJ, 316, 517

Sandage, A. 1993, AJ, 106, 703

Sandage, A., & Cacciari, C. 1990, ApJ, 350, 645

Sarajedini, A. 1994, AJ, 107, 618

Sarajedini, A., Lee, Y.-W., & Lee, D. H. 1995, ApJ, 450, 712

Schechter, P. L., Mateo, M., & Saha, A. 1993, PASP, 105, 1342

Stetson, P. B. 1994, PASP, 106, 250

Trauger, J. 1995, private communication

van den Bergh, S. 1995, ApJ, 451, L65

Walker, A. R. 1992, ApJ, 390, L81

Worthey, G. 1995, private communication

This preprint was prepared with the AAS LaTeX macros v4.0.

Fig. 1.— The Palomar Observatory Sky Survey red plate of M31 showing the locations of the four globular clusters studied.

Fig. 2.— The PC image of K58 through F555W. Shown are the 400 × 400 pixels ($18''.2 \times 18''.2$) centered on the cluster. The image is on a log scale.

Fig. 3.— The PC image of K105 through F555W. Shown are the 400 × 400 pixels ($18''.2 \times 18''.2$) centered on the cluster. The image is on a log scale.

Fig. 4.— The PC image of K108 through F555W. Shown are the 400 × 400 pixels ($18''.2 \times 18''.2$) centered on the cluster. The image is on a log scale.

Fig. 5.— The PC image of K219 through F555W. Shown are the 400 × 400 pixels ($18''.2 \times 18''.2$) centered on the cluster. The image is on a log scale.

Fig. 6.— Errors in fitted magnitudes of a simulated image as a function of magnitude. The plotted linear fit shows the small bias of < 0.01 mag introduced by DoPHOT over 5 magnitudes. This line was fitted to points brighter than $V = 25.5$; the dashed line divides the points which were fitted from those which were not. The squares show the errors in the manually obtained aperture magnitudes of the brightest group of stars ($V = 21.3$), offset by -0.2 mag in the abscissa as a visual aid.

Fig. 7.— Differences between input magnitudes and those measured by DoPHOT in simulated stars placed in the field of K219. Only stars beyond 128 pixels radius were used, so that background effects and crowding were small. The error bars represent the rms of the difference at each magnitude of the measured stars (~ 250 stars per magnitude bin). For further details see text.

Fig. 8.— The CMDs of K58. Only stars from 64 to 256 pixels are shown. The solid lines denote our estimate of 100% completeness. The number beneath the cluster label is the adopted [Fe/H].

Fig. 9.— The CMDs of K105. Only stars from 64 to 256 pixels are shown. The solid lines denote our estimate of 100% completeness. The number beneath the cluster label is the adopted [Fe/H].

Fig. 10.— The CMDs of K108. Only stars from 64 to 256 pixels are shown. The solid lines denote our estimate of 100% completeness. The number beneath the cluster label is the adopted [Fe/H].

Fig. 11.— The CMDs of K219. Only stars from 64 to 400 pixels are shown. The solid lines denote our estimate of 100% completeness. The number beneath the cluster label is the adopted [Fe/H].

Fig. 12.— The CMDs of K58 in six annuli. The radii are given in pixels.

Fig. 13.— The CMDs of K105 in six annuli. The radii are given in pixels.

Fig. 14.— The CMDs of K108 in six annuli. The radii are given in pixels.

Fig. 15.— The CMDs of K219 in six annuli. The radii are given in pixels.

Fig. 16.— The V luminosity function of K58. The ordinate is on a log scale. The solid histogram is the entire LF. The solid curve is the smoothed, normalized background LF. The bins are 0.04 mag wide. The mean of the HB "red clump" provides the level of the HB and is determined by a parabolic fit (in magnitude coordinates).

Fig. 17.— The RGB of K219. The left panel shows the CMD with the trace of the RGB ridge line. The right panel, which has a different horizontal scaling, shows the RGB ridge line with the standard giant branches of M15 ([Fe/H]= −2.17) and N6397 ([Fe/H]= −1.91) shifted and superposed for comparison.

Fig. 18.— The RGB of K105. The left panel shows the CMD with the trace of the RGB ridge line. The right panel, which has a different horizontal scaling, shows the RGB ridge line with the standard giant branches of N6397 ([Fe/H]= −1.91) and N6752 ([Fe/H]= −1.54) shifted and superposed for comparison.

Fig. 19.— The RGB of K58. The left panel shows the CMD with the trace of the RGB ridge line. The right panel, which has a different horizontal scaling, shows the RGB ridge line with the standard giant branch of 47 Tuc ([Fe/H]= −0.71) shifted and superposed for comparison.

Fig. 20.— The RGB of K108. The left panel shows the CMD with the trace of the RGB ridge line. The right panel, which has a different horizontal scaling, shows the RGB ridge line with the standard giant branches of 47 Tuc ([Fe/H]= −0.71) and N1851 ([Fe/H]= −1.29) shifted and superposed for comparison.

Fig. 21.— The RGB of the K58 Field is shown in the WFPC-2 flight system. Open circles represent an isochrone at 10 Gyr and [Fe/H] = −0.50. Open squares represent an isochrone at 5 Gyr and [Fe/H] = −0.225. Open triangles represent an isochrone at 2 Gyr and [Fe/H] = +0.00.

Fig. 22.— The RGB of the K108 Field is shown in the WFPC-2 flight system. Open circles represent two isochrones at 10 Gyr and bracketing [Fe/H] = −0.50 and −0.25. Open squares represent two isochrones at 5 Gyr and bracketing [Fe/H] = −0.225 and +0.00. Open triangles represent two isochrones at 2 Gyr and bracketing [Fe/H] = +0.00 and +0.25.

Fig. 23.— The RGB ridge lines of all clusters after extinction correction.

Fig. 24.— The dereddened RR Lyrae magnitudes of the clusters and M31 fields. The line (equation 9) indicates the best fit to the three GCs, indicated by the filled circles.

Fig. 1

Fig. 1

K108
K58
K105
K219

Fig. 2

Fig. 2

K58

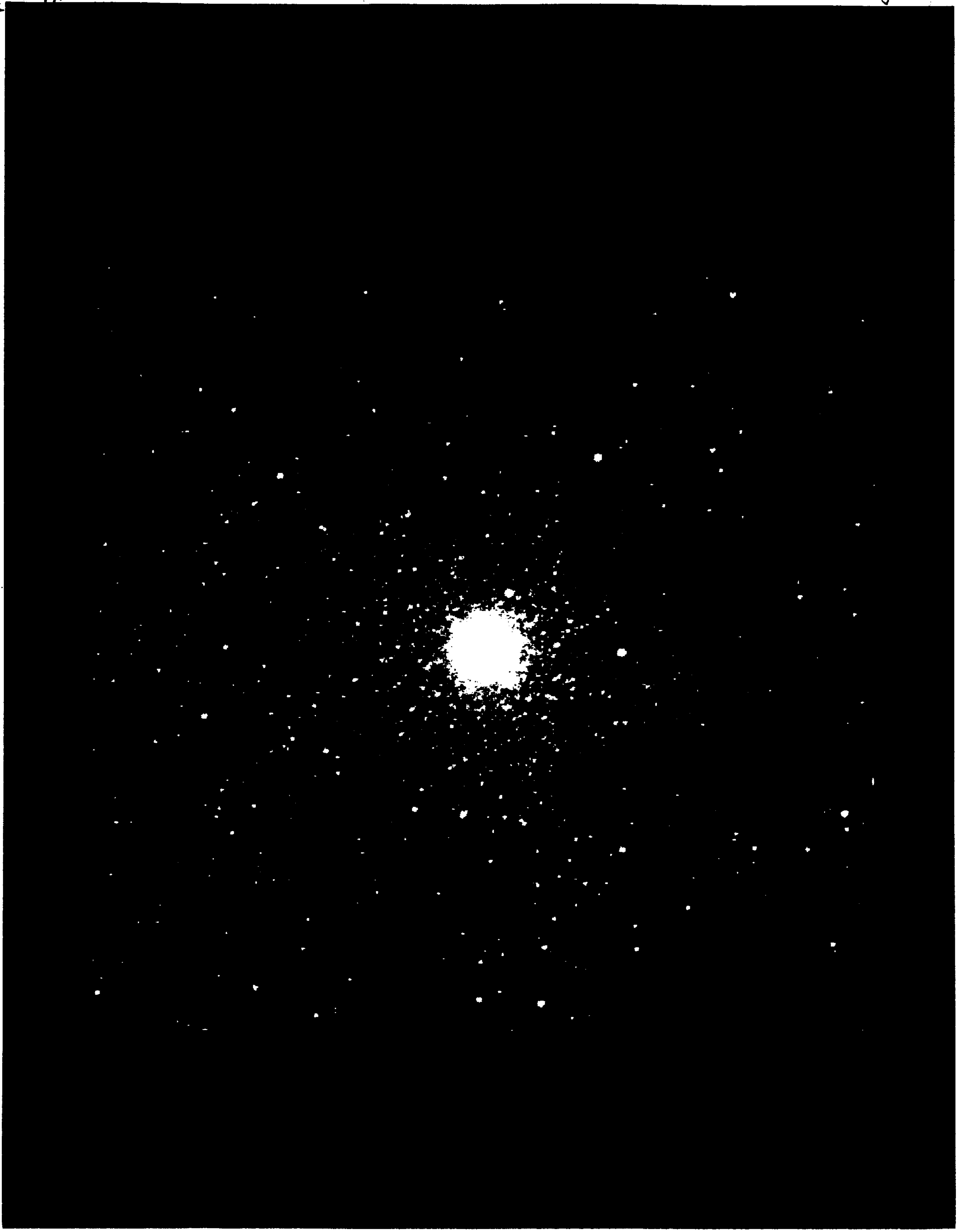

← Fig. 3

Fig. 3

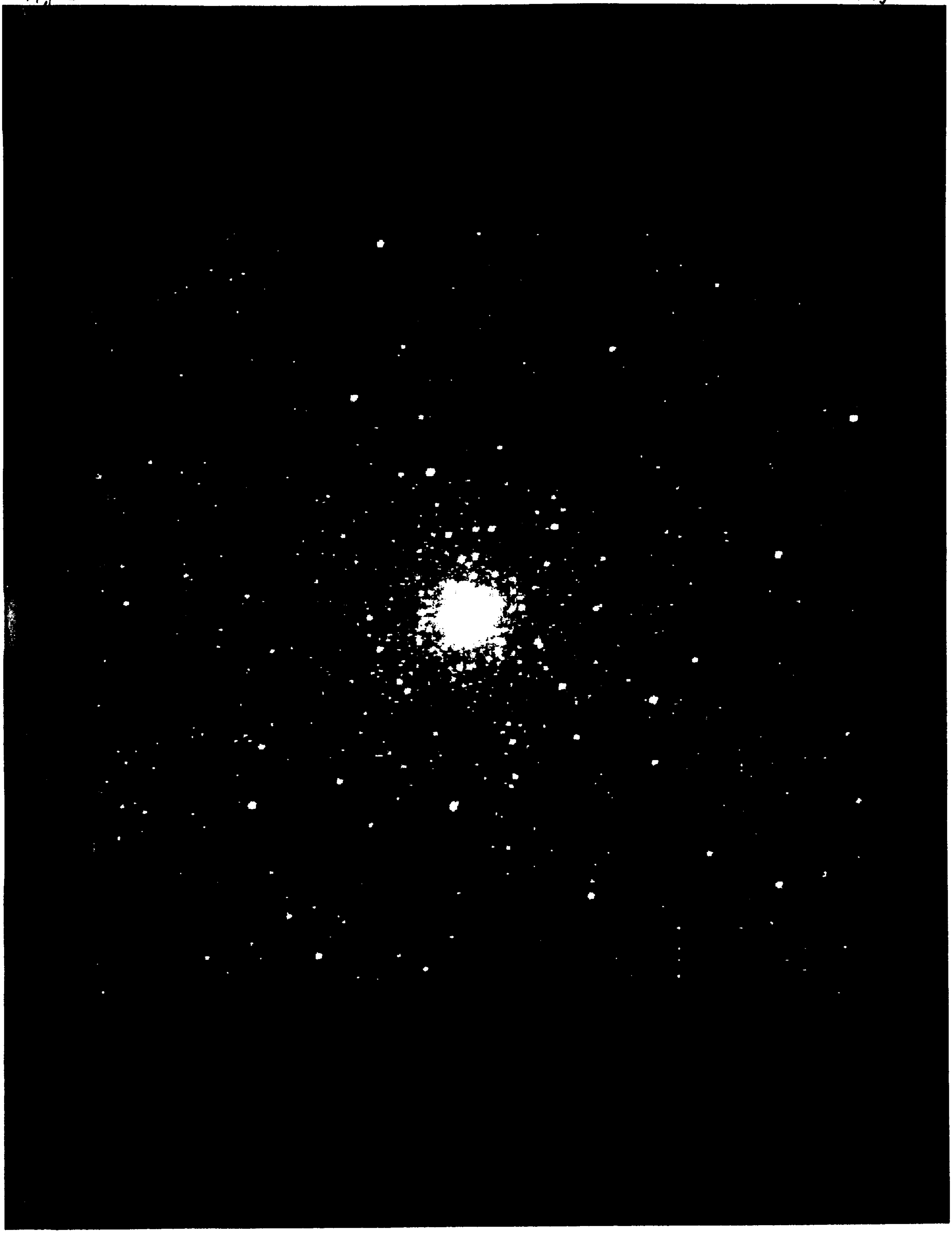

← Fig. 4

Fig. 4.

8017

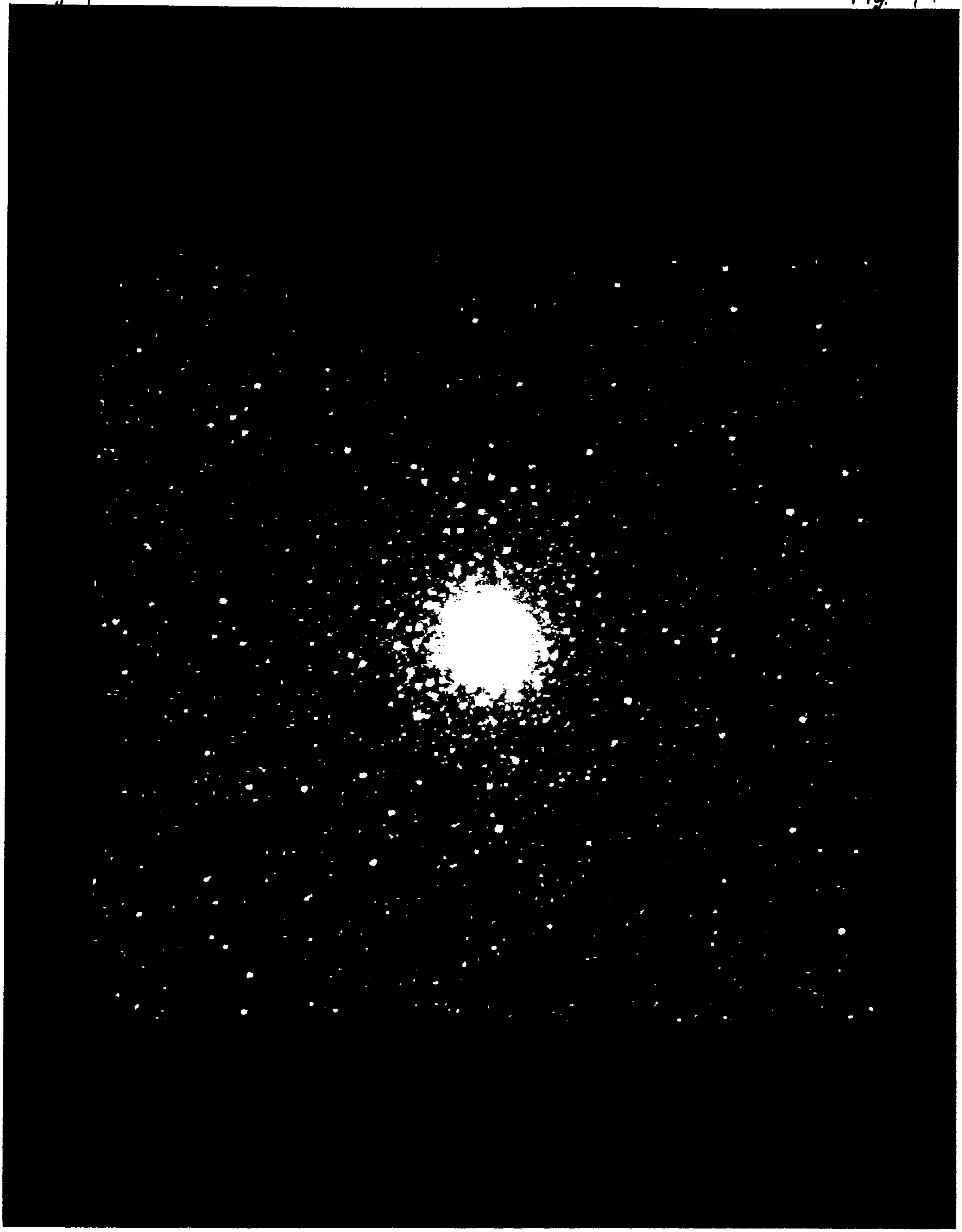

← Fig. 5

Fig. 5

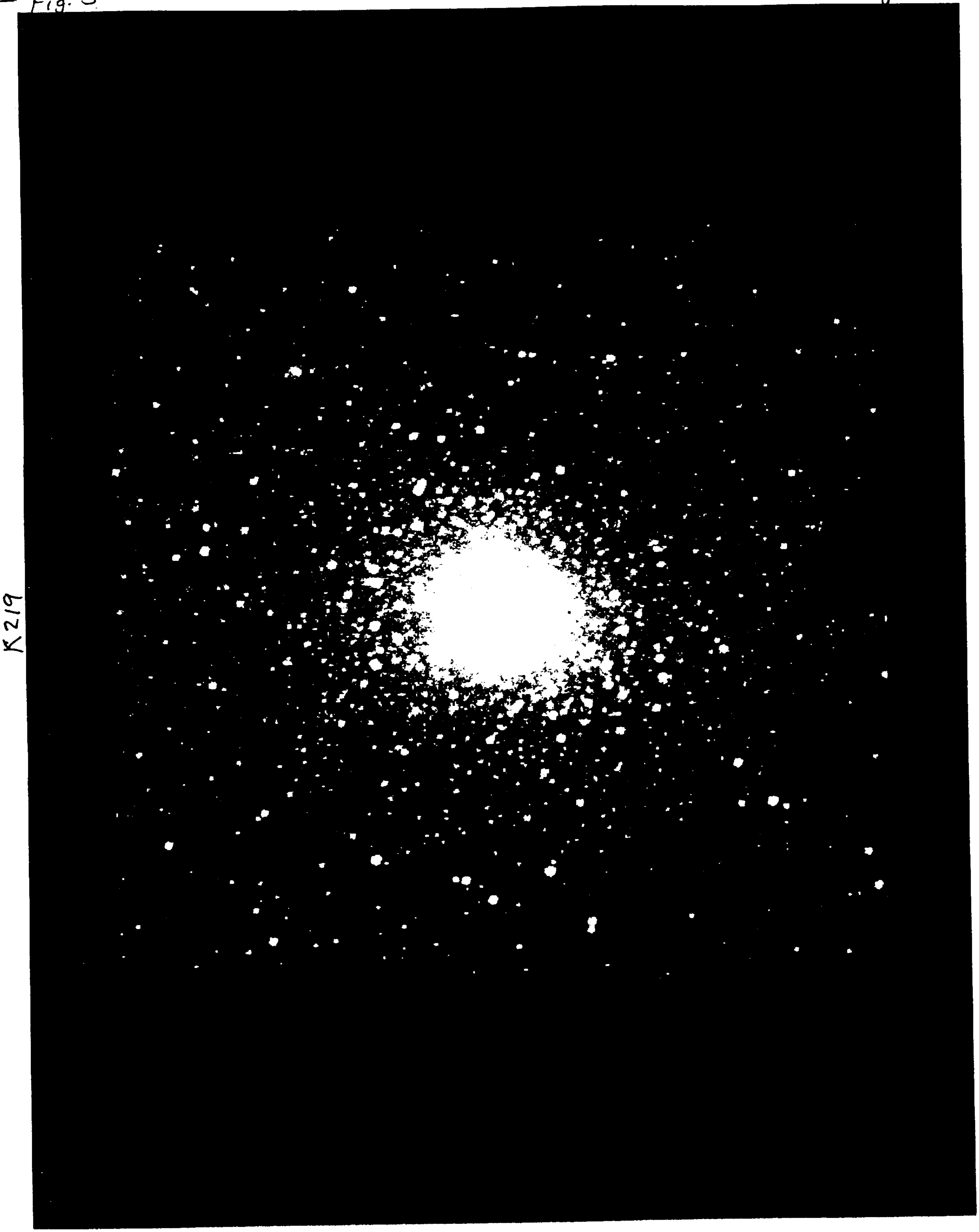

K219

Fig. 6

Fig. 6

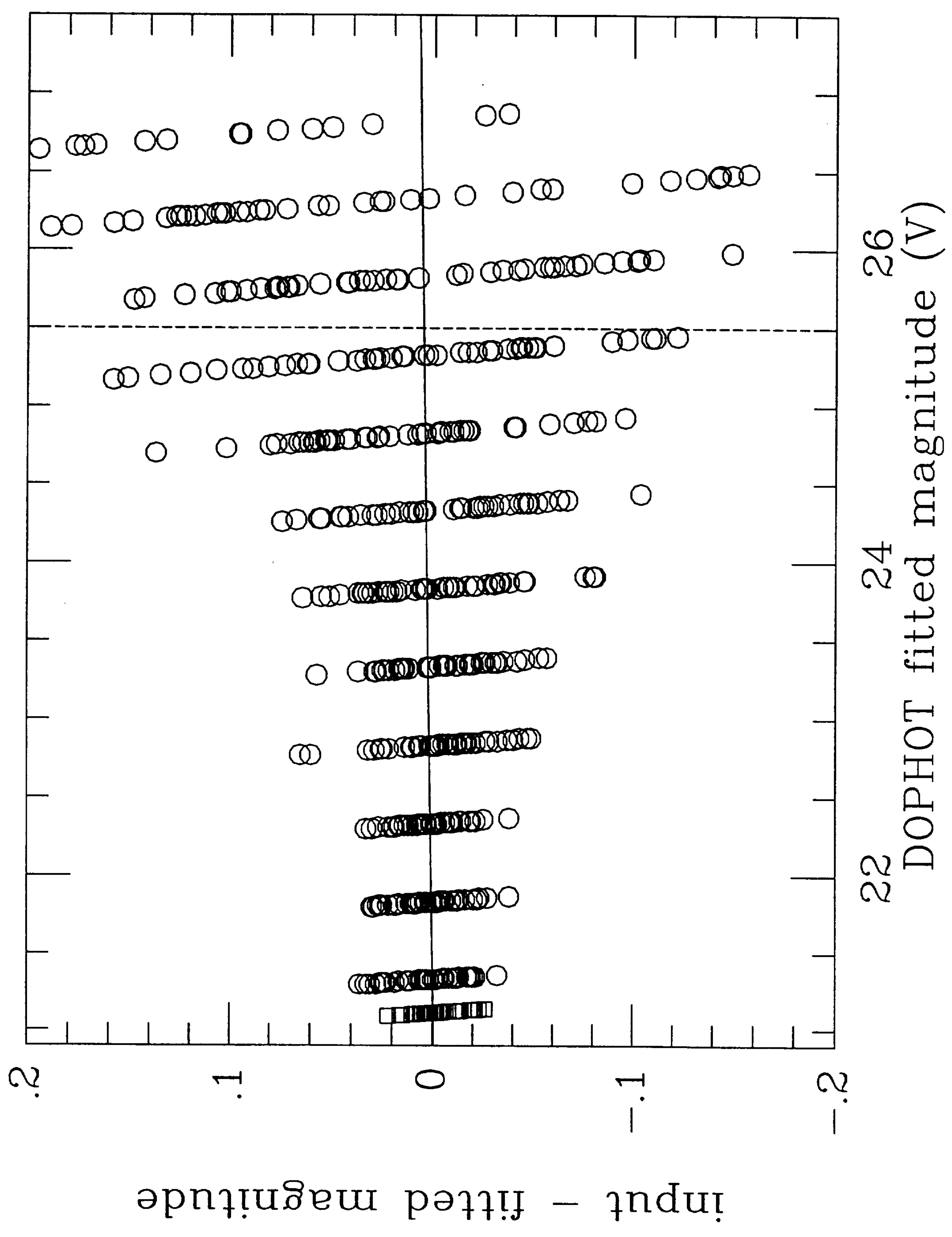

22
24
26
DOPHOT fitted magnitude (V)
.2
.1
0
-.1
-.2
input − fitted magnitude

Fig. 7 Fig. 7

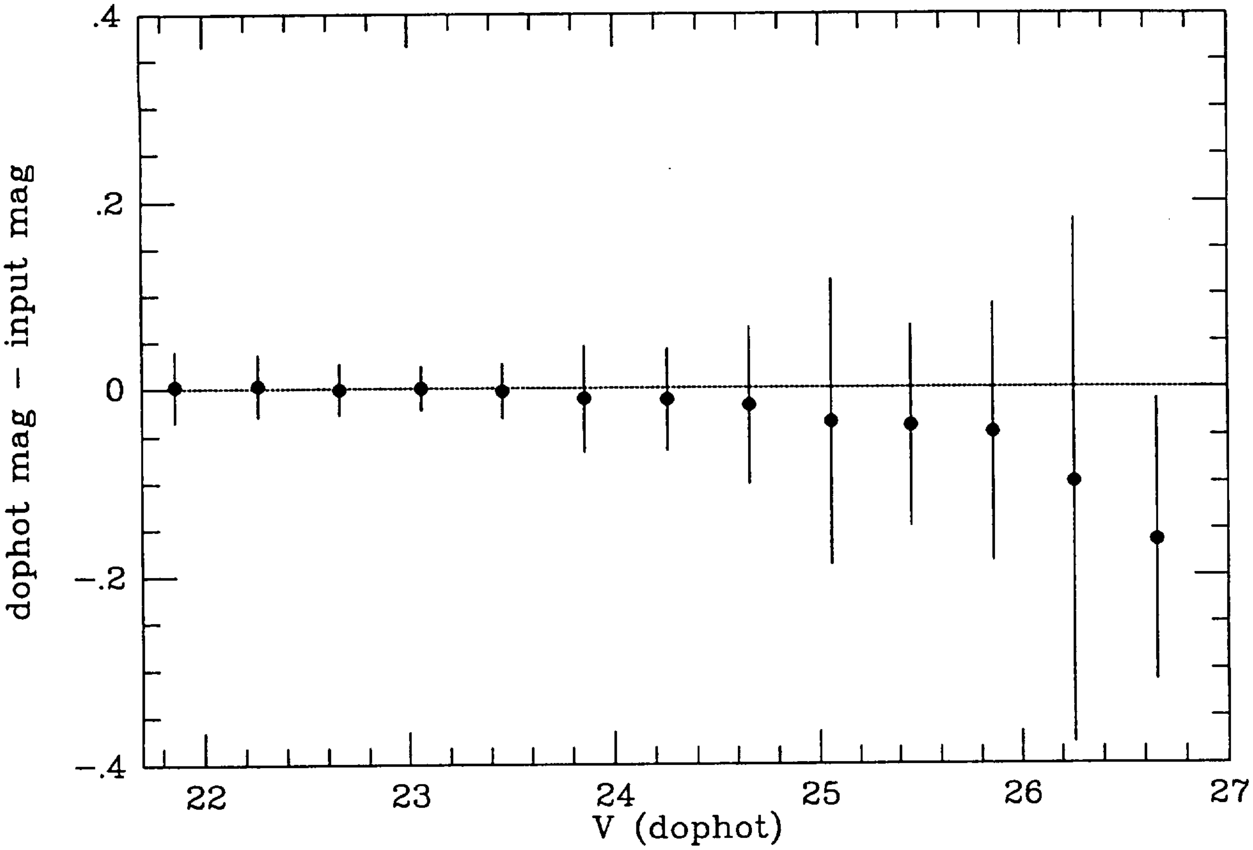

.4
.2
0
-.2
-.4
dophot mag - input mag
22
23
24
25
26
27
V (dophot)

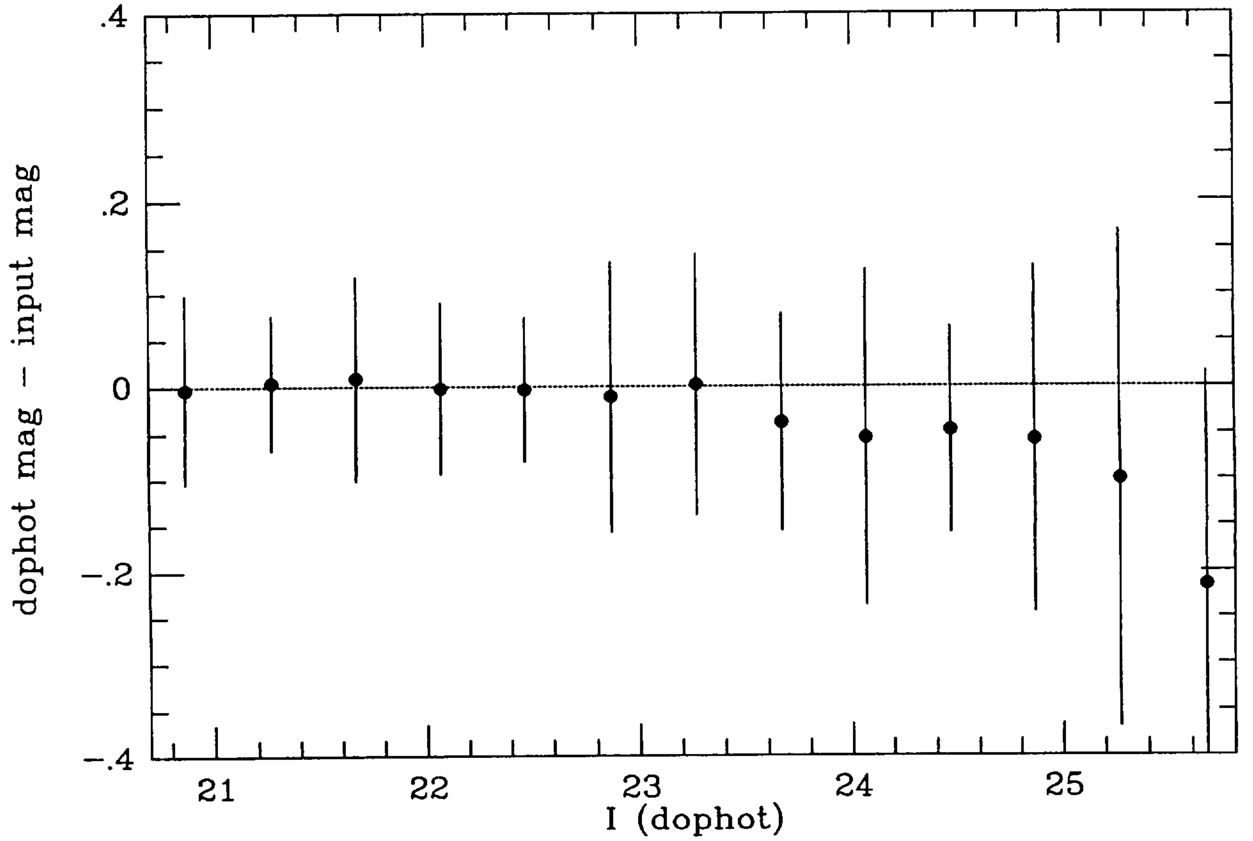

.4
.2
0
-.2
-.4
dophot mag - input mag
21
22
23
24
25
I (dophot)

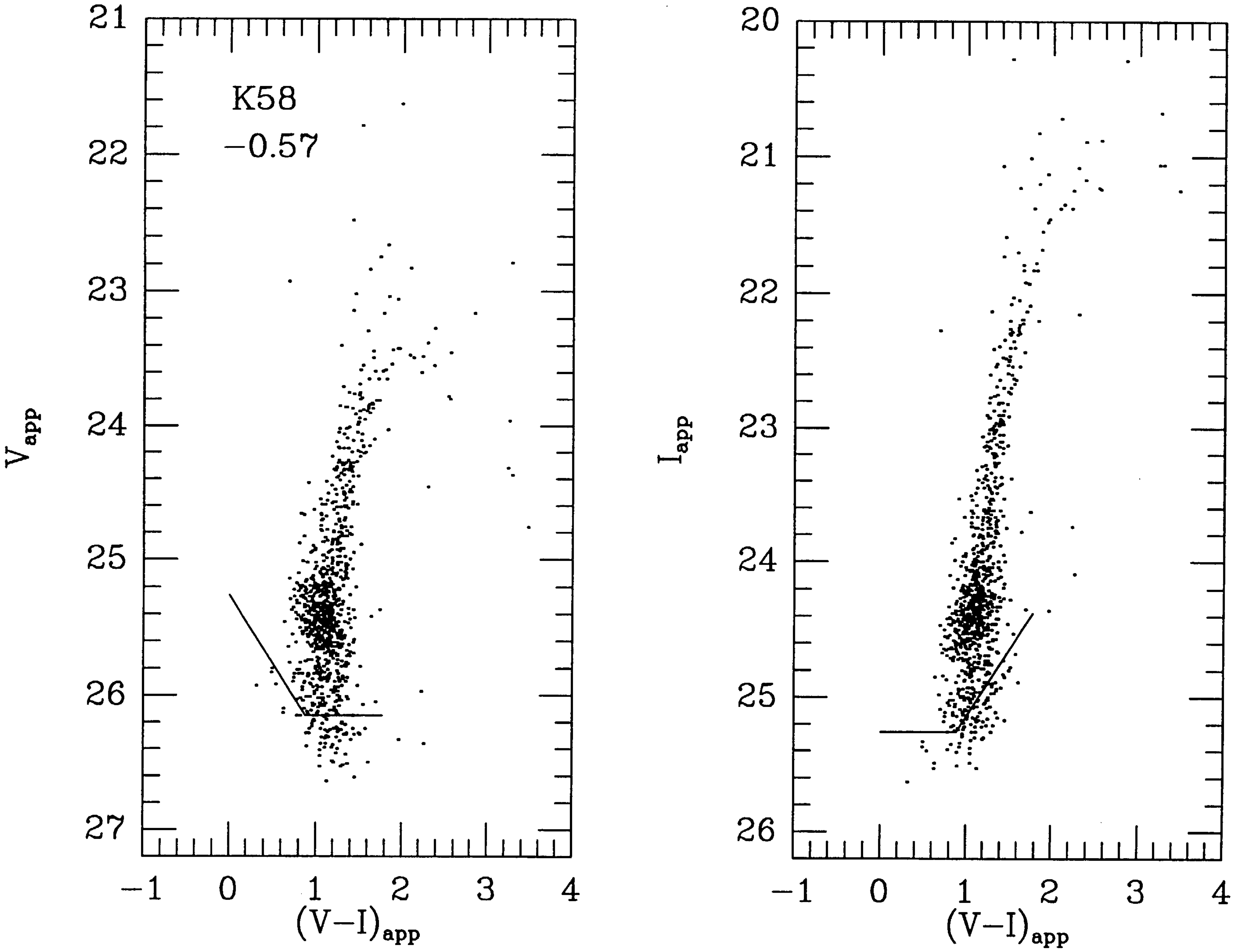
K58
−0.57
V_{app}
21
22
23
24
25
26
27
−1
0
1
2
3
4
$(V-I)_{app}$
I_{app}
20
21
22
23
24
25
26
−1
0
1
2
3
4
$(V-I)_{app}$

Fig. 8

Fig. 8

Fig. 9

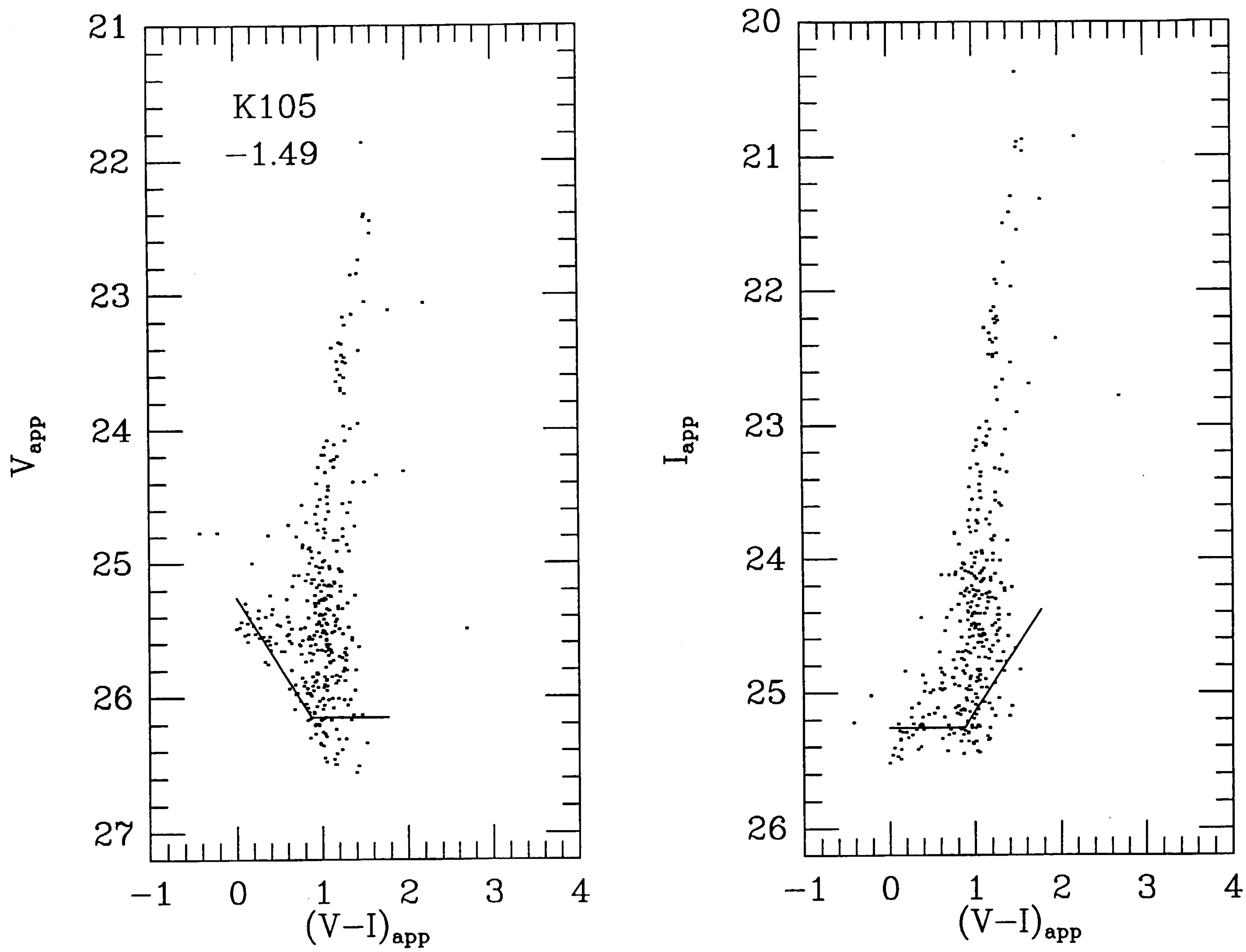

K105
−1.49
V_{app}
21
22
23
24
25
26
27
−1
0
1
2
3
4
$(V-I)_{app}$
I_{app}
20
21
22
23
24
25
26
−1
0
1
2
3
4
$(V-I)_{app}$

Fig. 9

Fig. 10

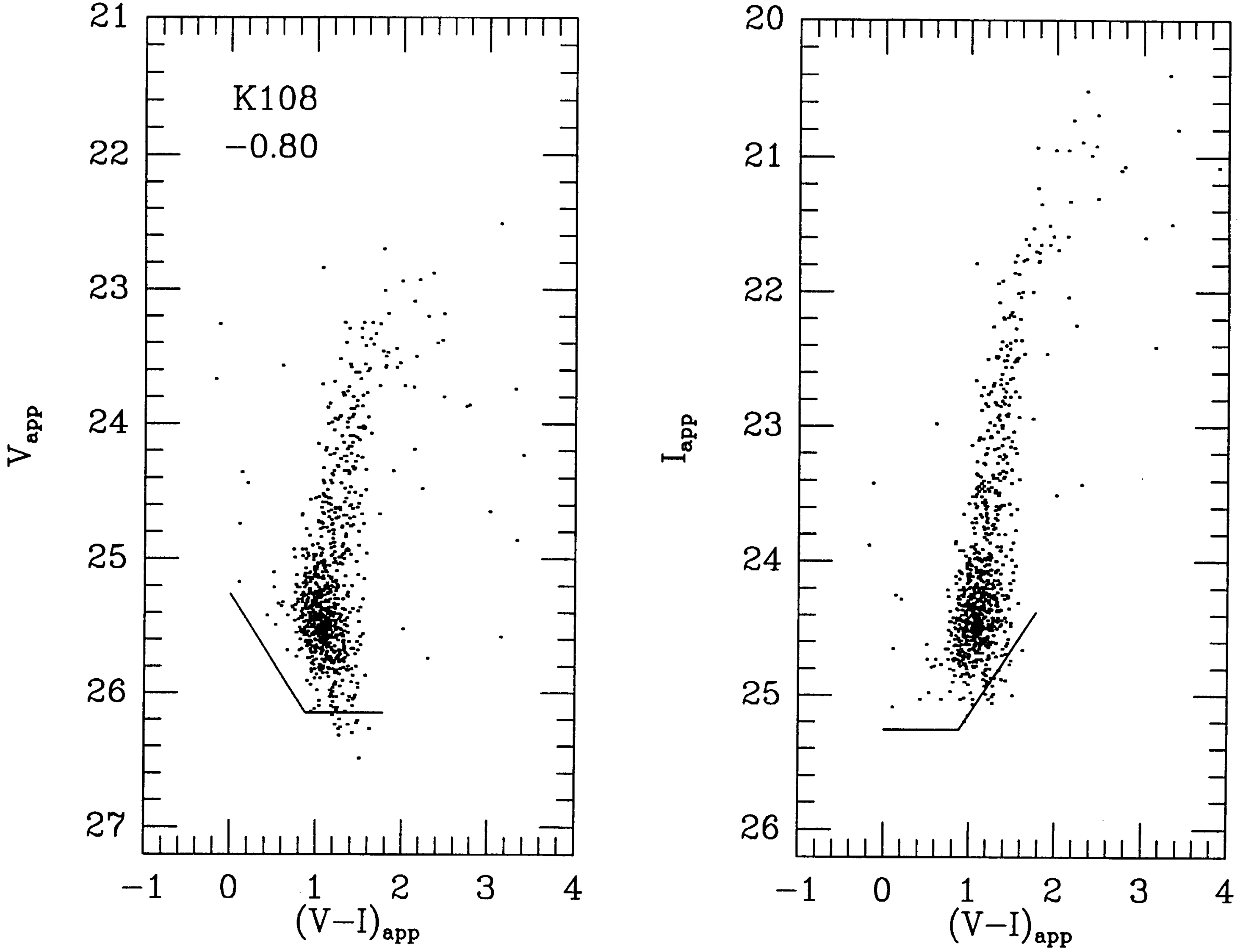
K108
−0.80
21
22
23
24
25
26
27
V_{app}
−1
0
1
2
3
4
$(V-I)_{app}$
20
21
22
23
24
25
26
I_{app}
−1
0
1
2
3
4
$(V-I)_{app}$

Fig. 10

Fig. 11

Fig. 11

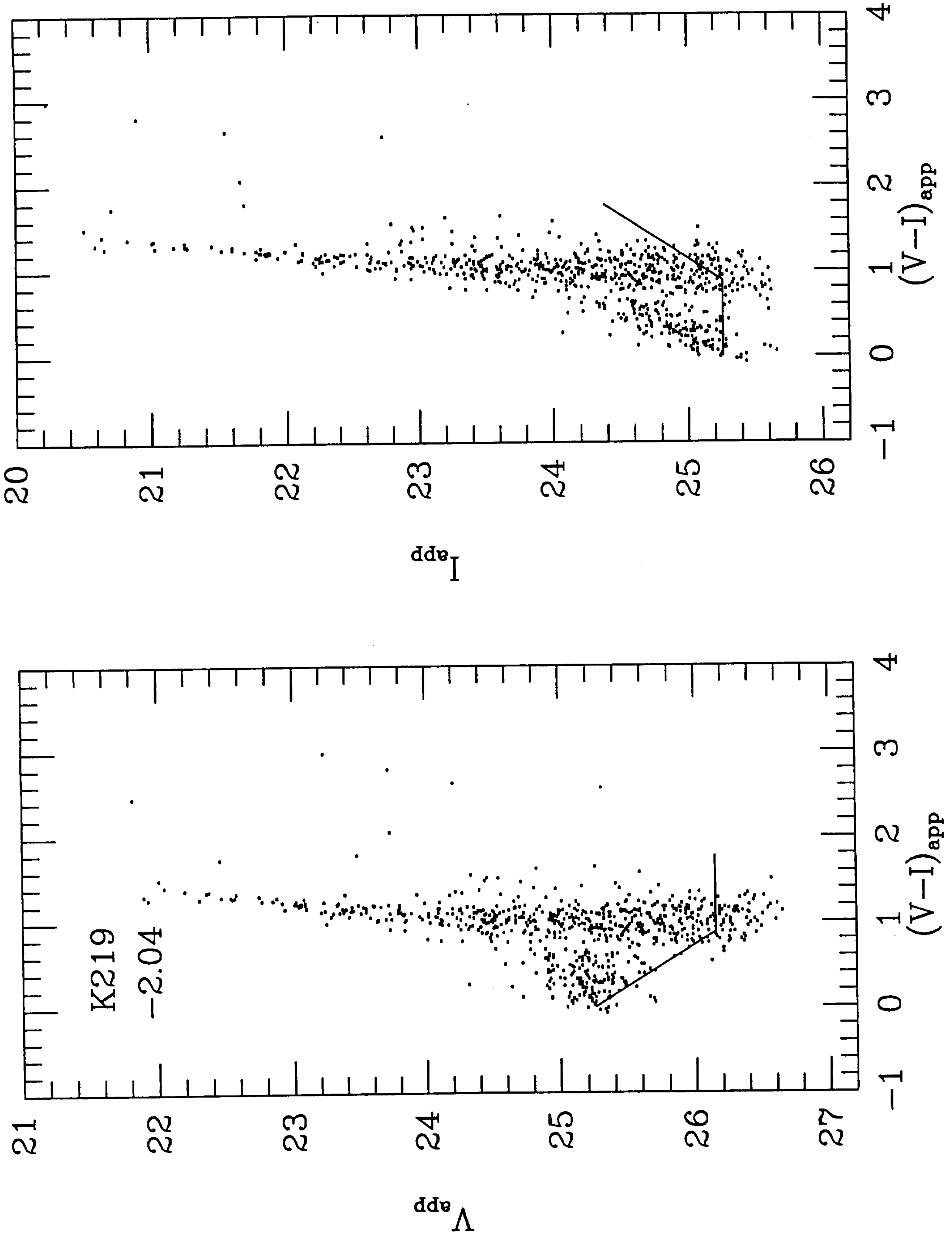
K219
−2.04
V_app
21
22
23
24
25
26
27
I_app
20
21
22
23
24
25
26
(V−I)_app
−1
0
1
2
3
4

Fig. 12

Fig. 12

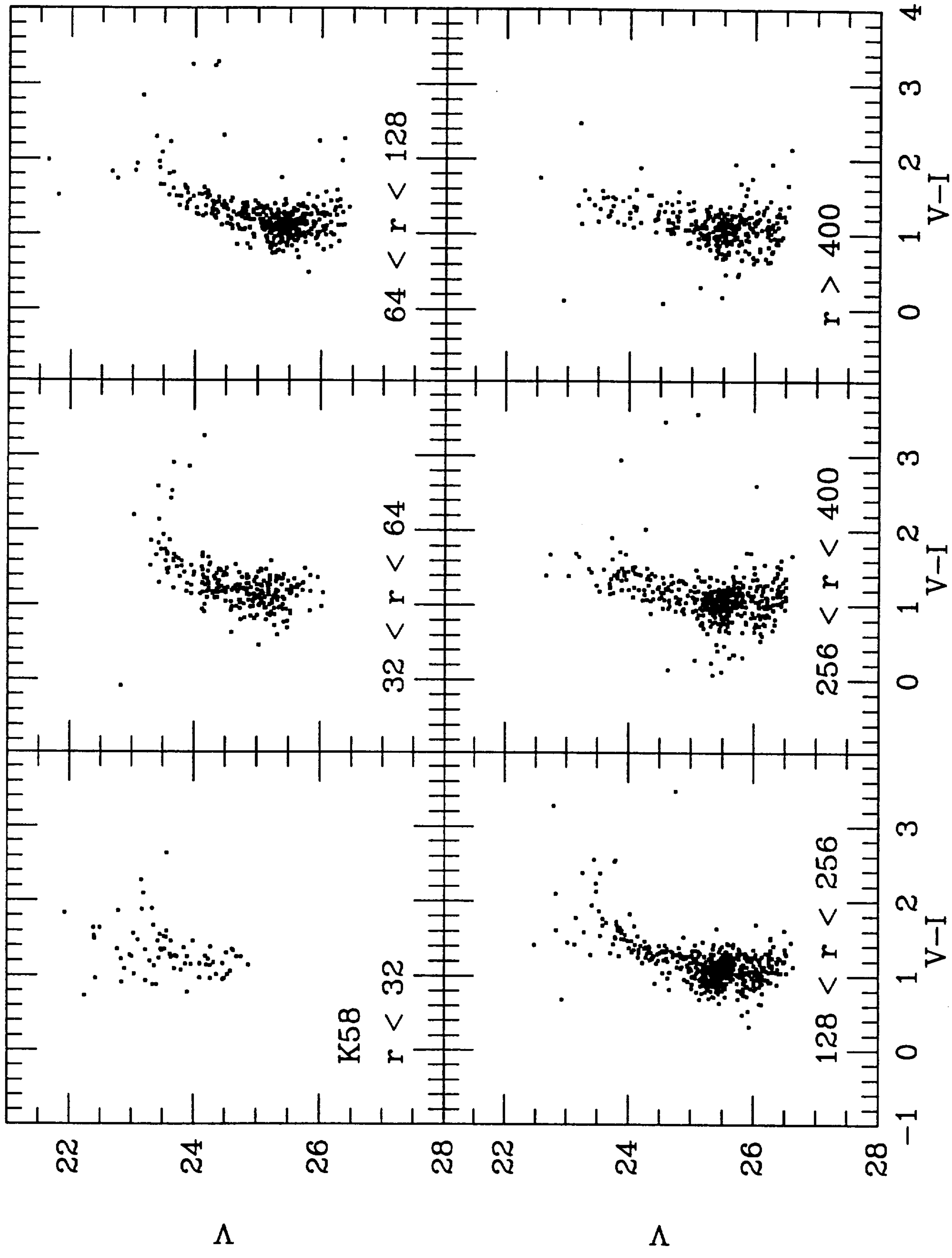

K58
r < 32
32 < r < 64
64 < r < 128
128 < r < 256
256 < r < 400
r > 400
V
V
V−I
V−I
V−I
22
24
26
28
22
24
26
28
−1
0
1
2
3
4

Fig. 13

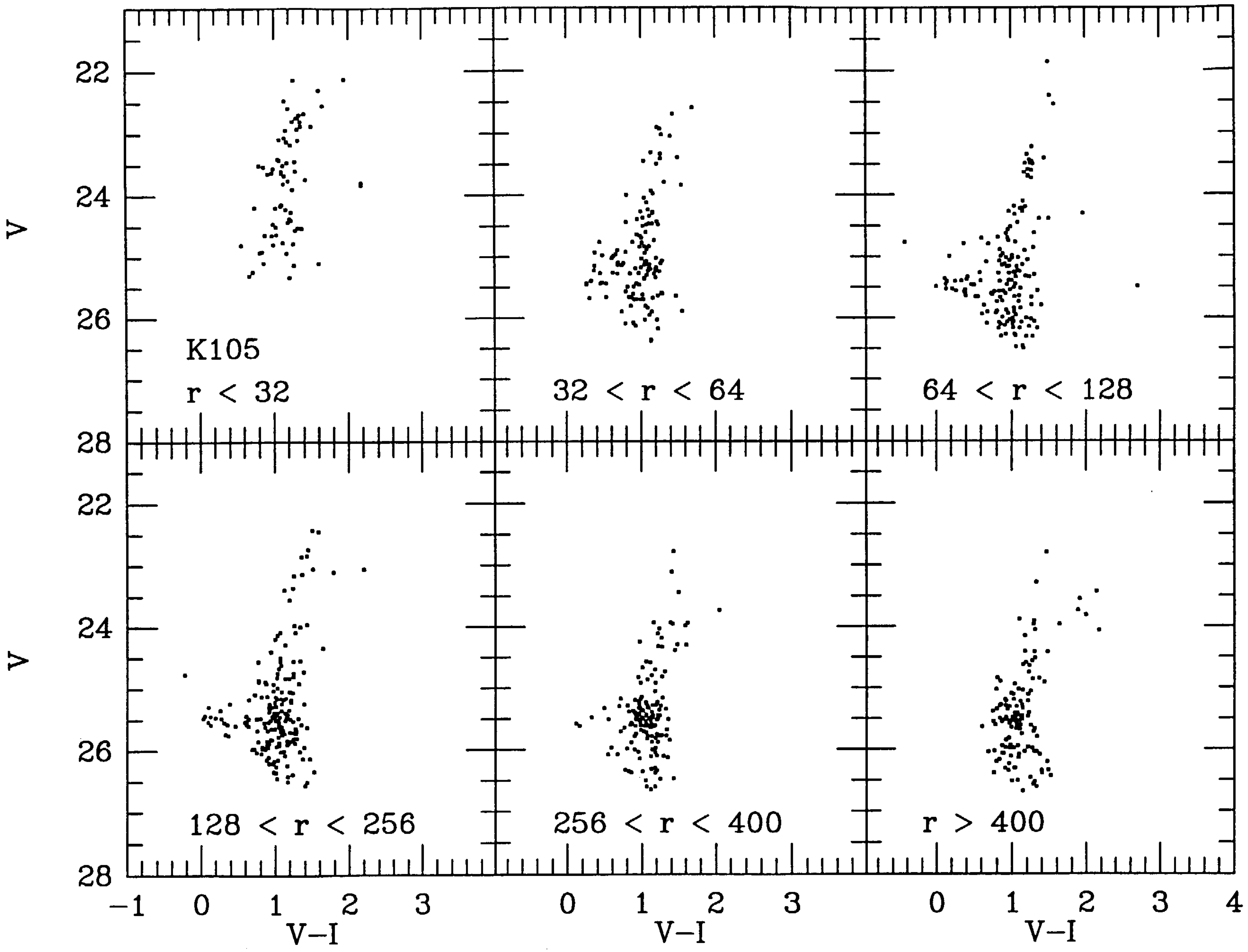
K105
r < 32
32 < r < 64
64 < r < 128
128 < r < 256
256 < r < 400
r > 400
V
22
24
26
28
V
22
24
26
28
−1
0
1
2
3
V−I
0
1
2
3
V−I
0
1
2
3
4
V−I

Fig. 13

Fig. 14

Fig. 14

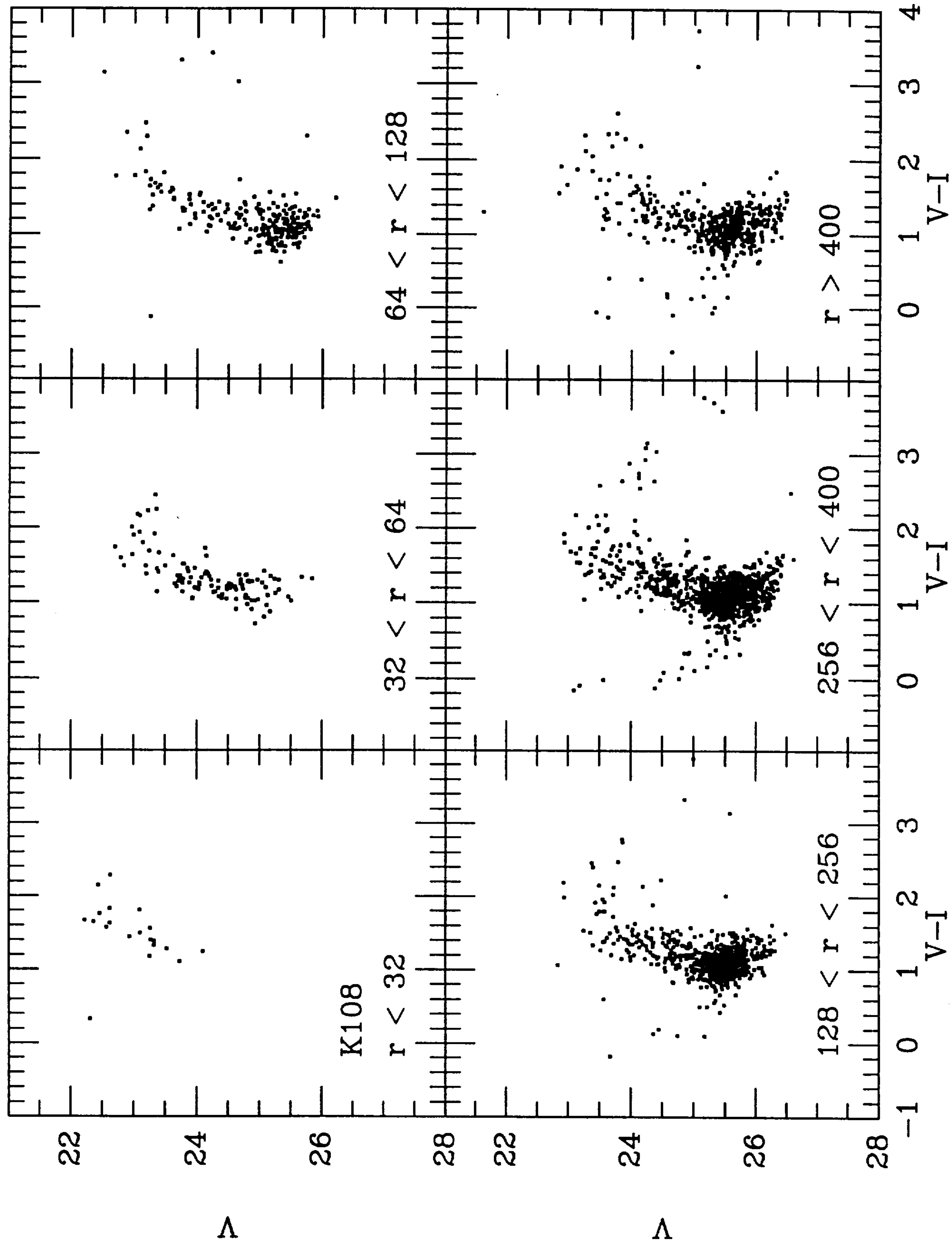

K108
r < 32
32 < r < 64
64 < r < 128
128 < r < 256
256 < r < 400
r > 400
V
V
V−I
V−I
V−I
22
24
26
28
22
24
26
28
−1
0
1
2
3
4

Fig. 15

Fig. 15

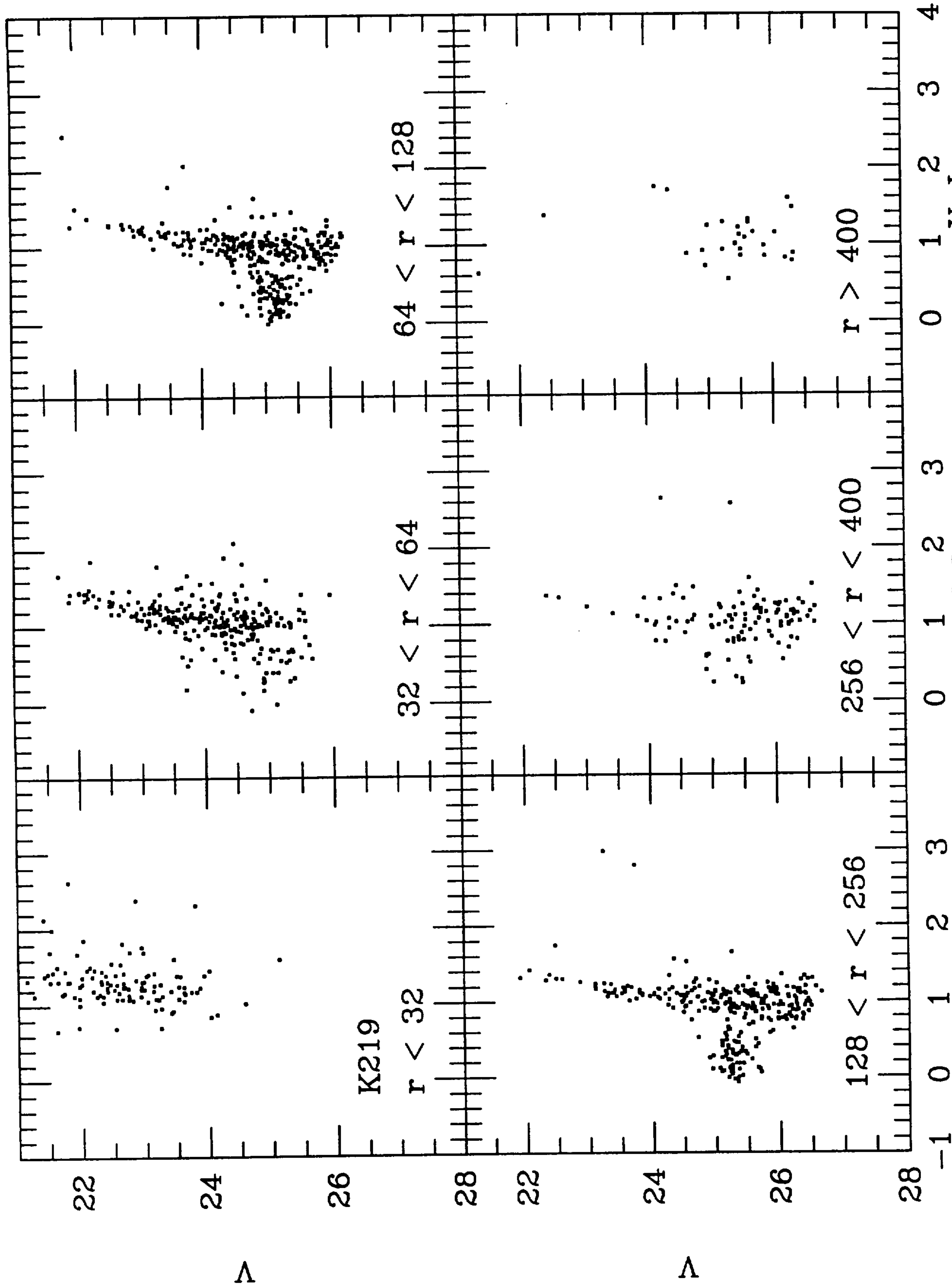
K219
r < 32
32 < r < 64
64 < r < 128
128 < r < 256
256 < r < 400
r > 400
V−I
V
22
24
26
28
−1
0
1
2
3
4

Fig. 16

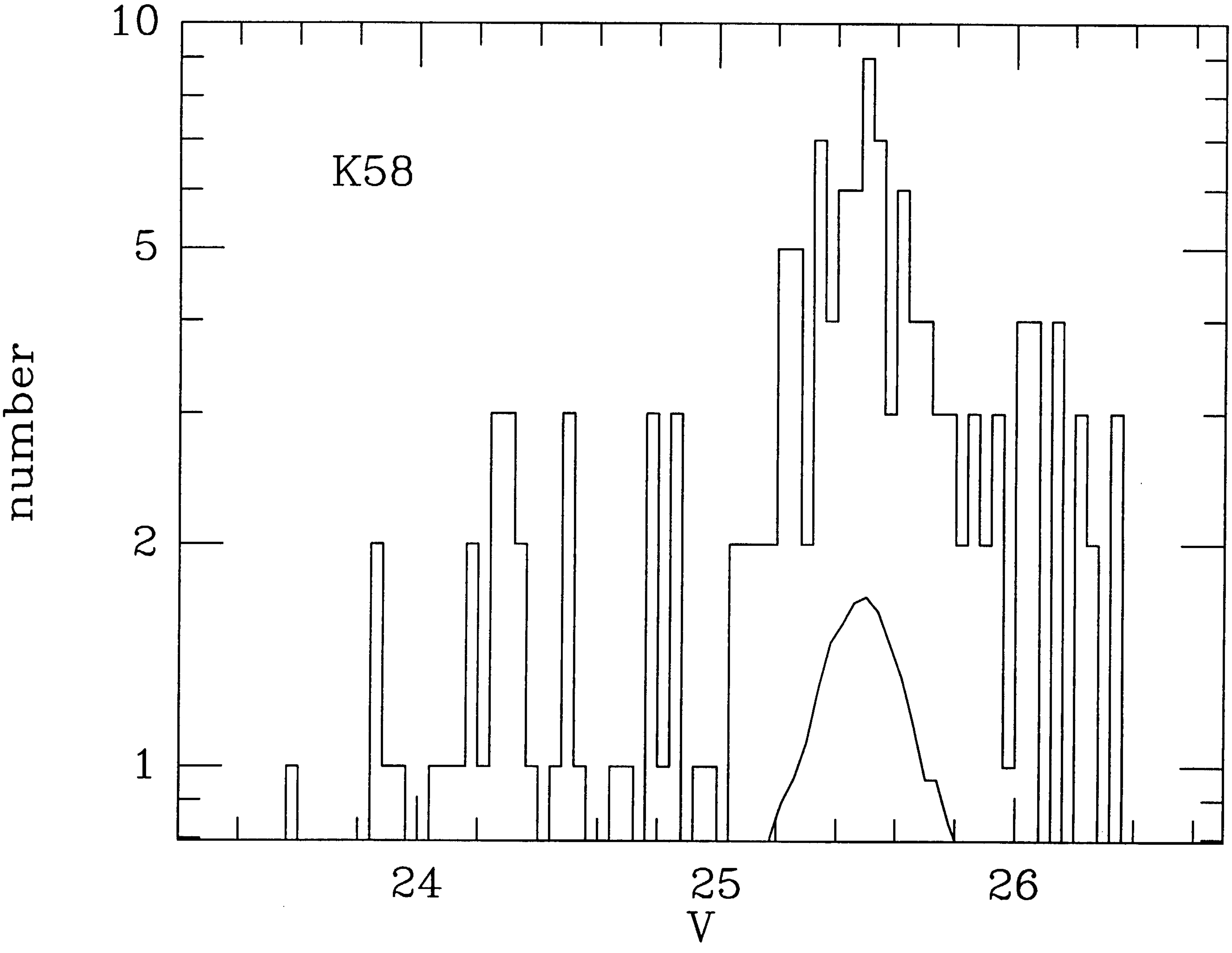

Fig. 16

Fig. 17

Fig. 17

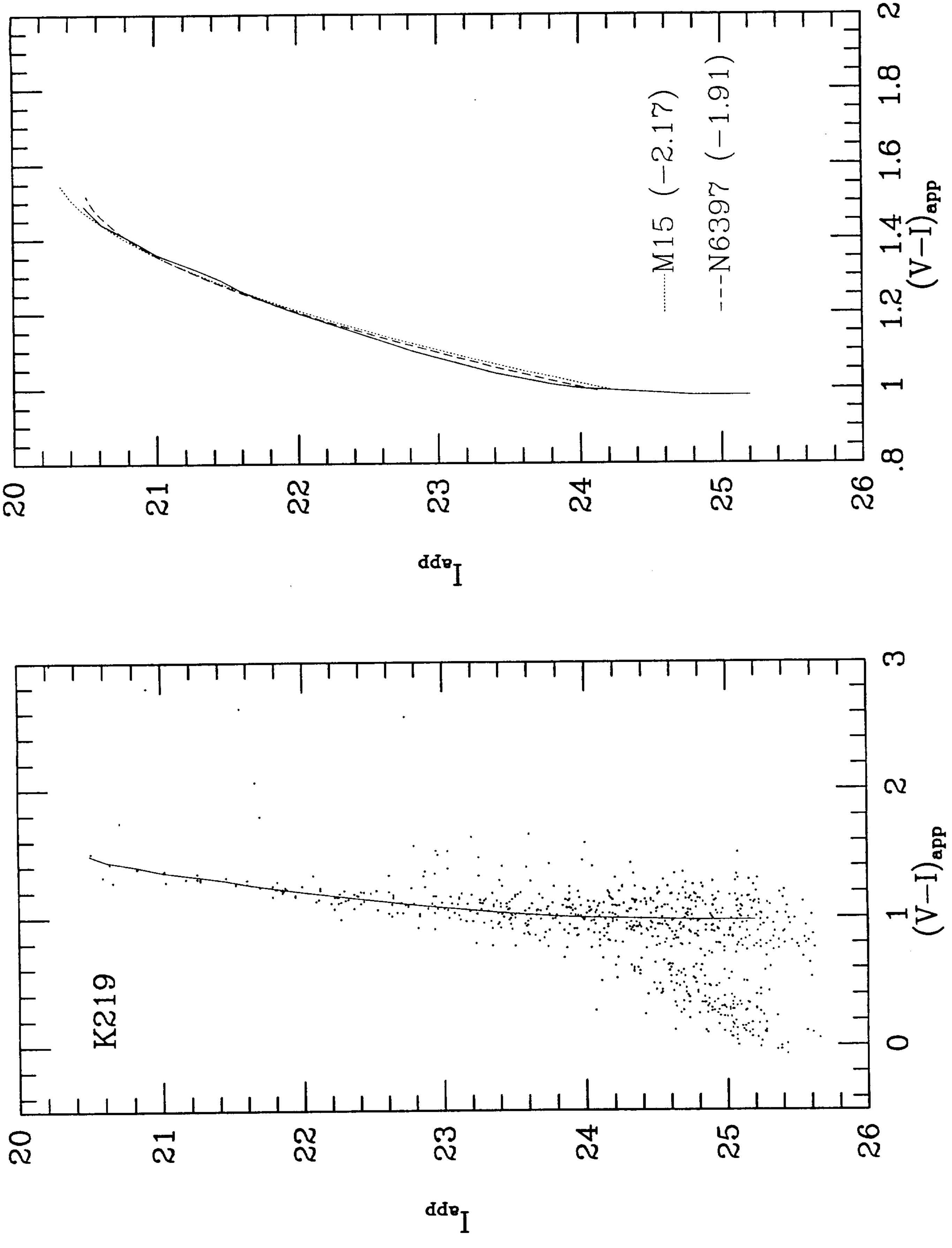

K219
I_{app}
$(V-I)_{app}$
20
21
22
23
24
25
26
0
1
2
3
—M15 (−2.17)
---N6397 (−1.91)
.8
1
1.2
1.4
1.6
1.8
2

Fig. 18

Fig. 18

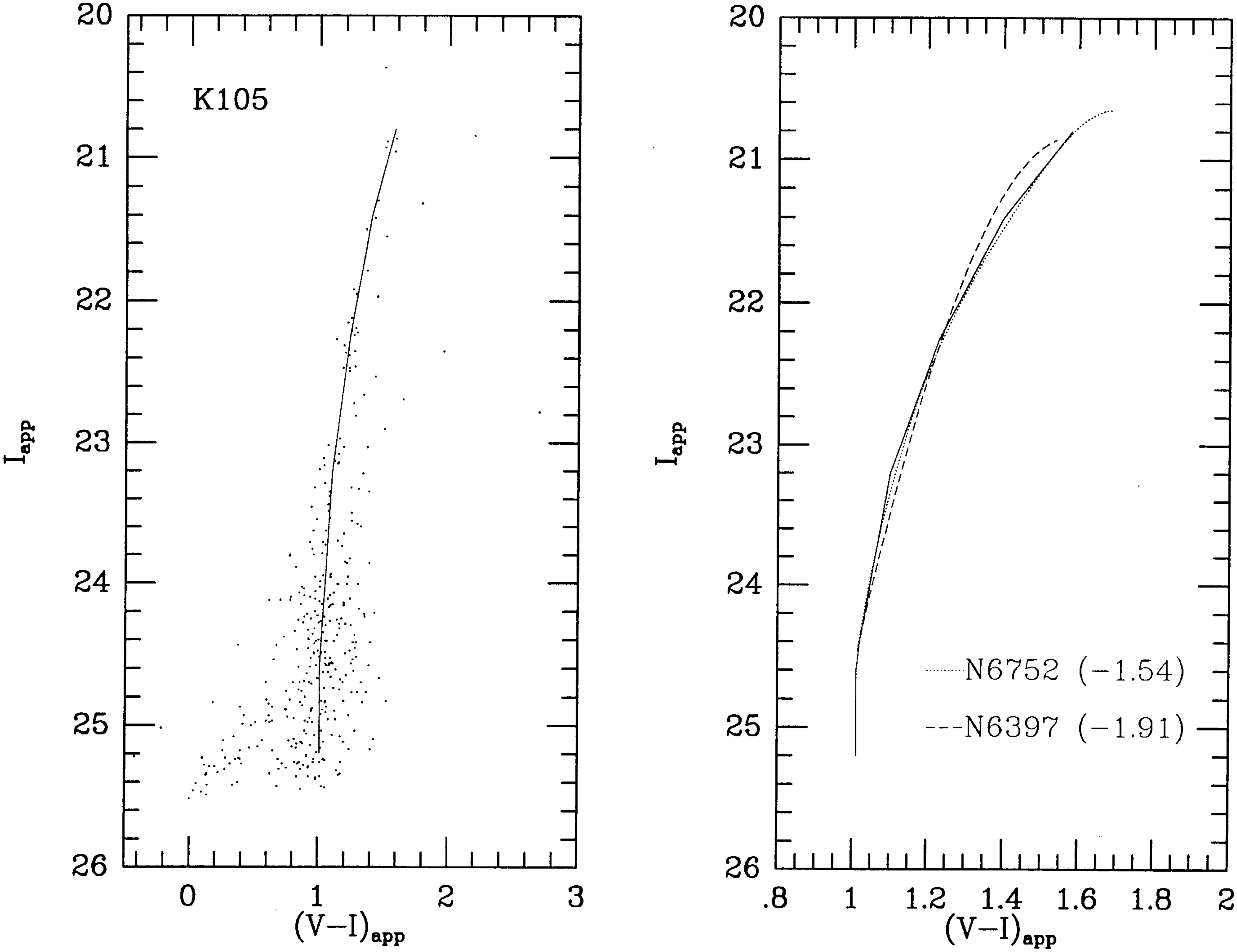
K105
I_app
20
21
22
23
24
25
26
0
1
2
3
(V−I)_app
I_app
.8
1
1.2
1.4
1.6
1.8
2
(V−I)_app
N6752 (−1.54)
N6397 (−1.91)

Fig. 19

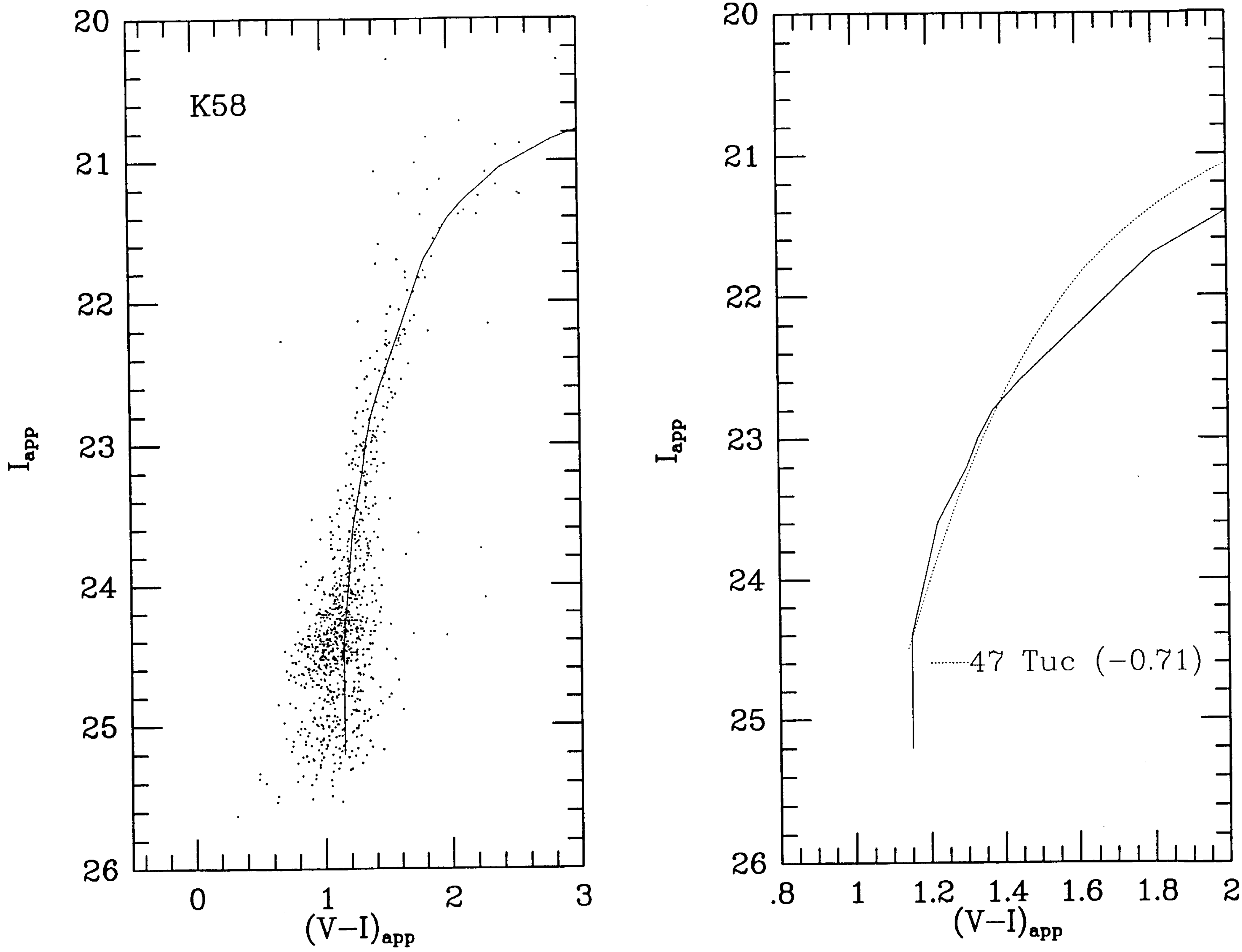

Fig. 19

Fig. 20

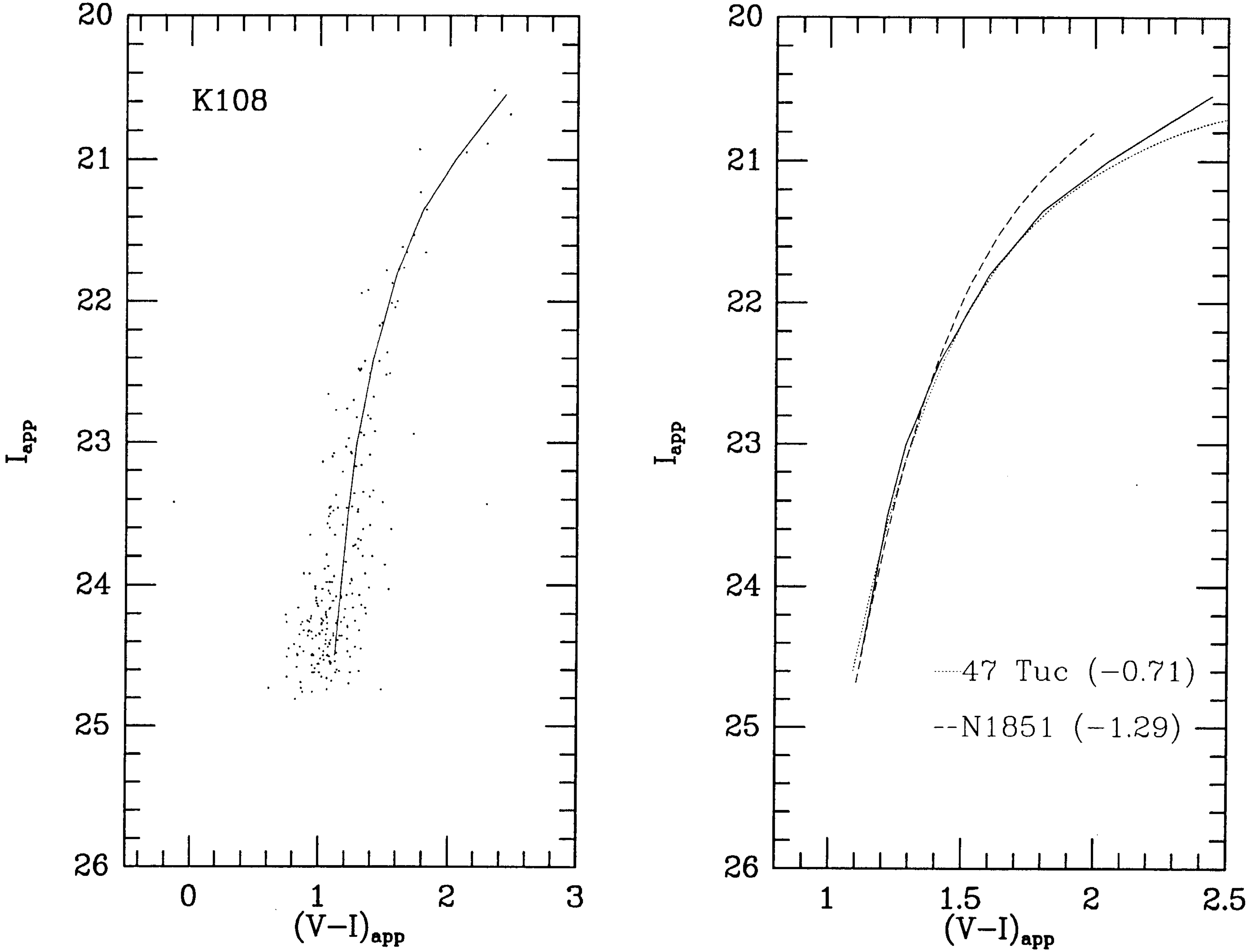
K108
I_{app}
20
21
22
23
24
25
26
0
1
2
3
$(V-I)_{app}$
I_{app}
1
1.5
2
2.5
$(V-I)_{app}$
47 Tuc (−0.71)
N1851 (−1.29)

Fig. 20

Fig. 21

Fig. 21

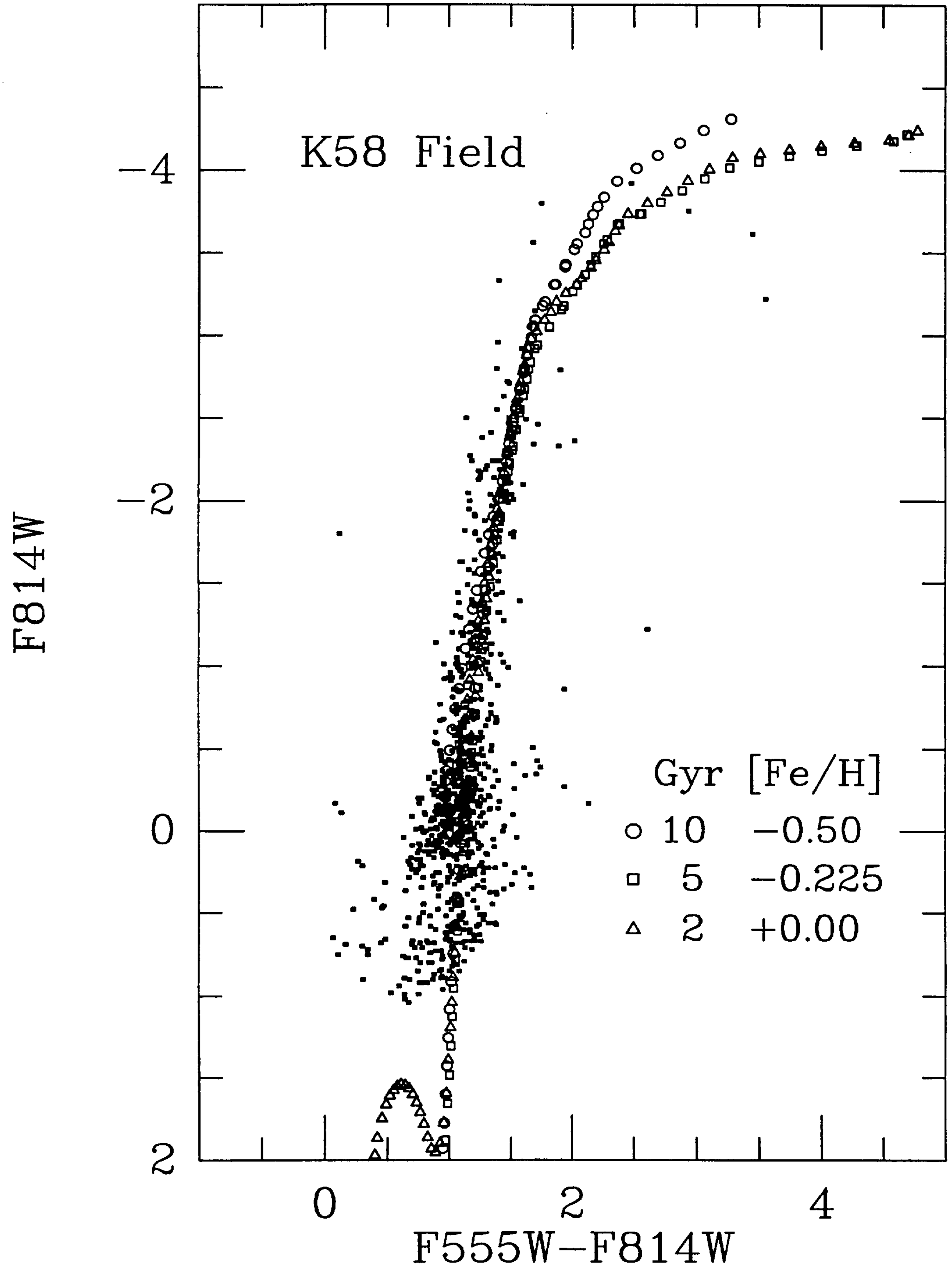
K58 Field
F814W
F555W−F814W
−4
−2
0
2
0
2
4
Gyr [Fe/H]
○ 10 −0.50
□ 5 −0.225
△ 2 +0.00

Fig. 22 Fig. 22

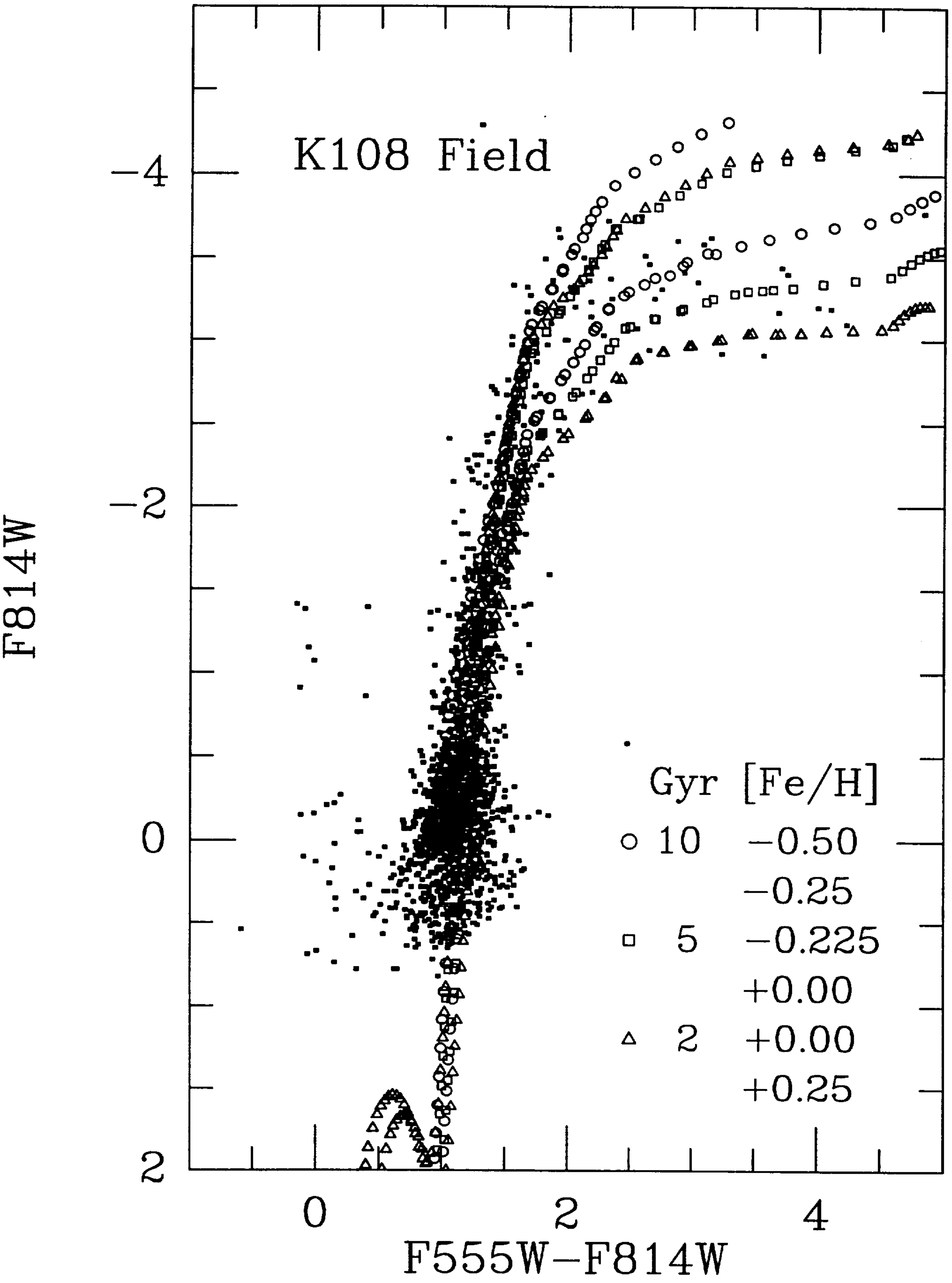
K108 Field
F814W
F555W−F814W
−4
−2
0
2
0
2
4
Gyr [Fe/H]
○ 10 −0.50
−0.25
□ 5 −0.225
+0.00
△ 2 +0.00
+0.25

Fig. 23

Fig. 23

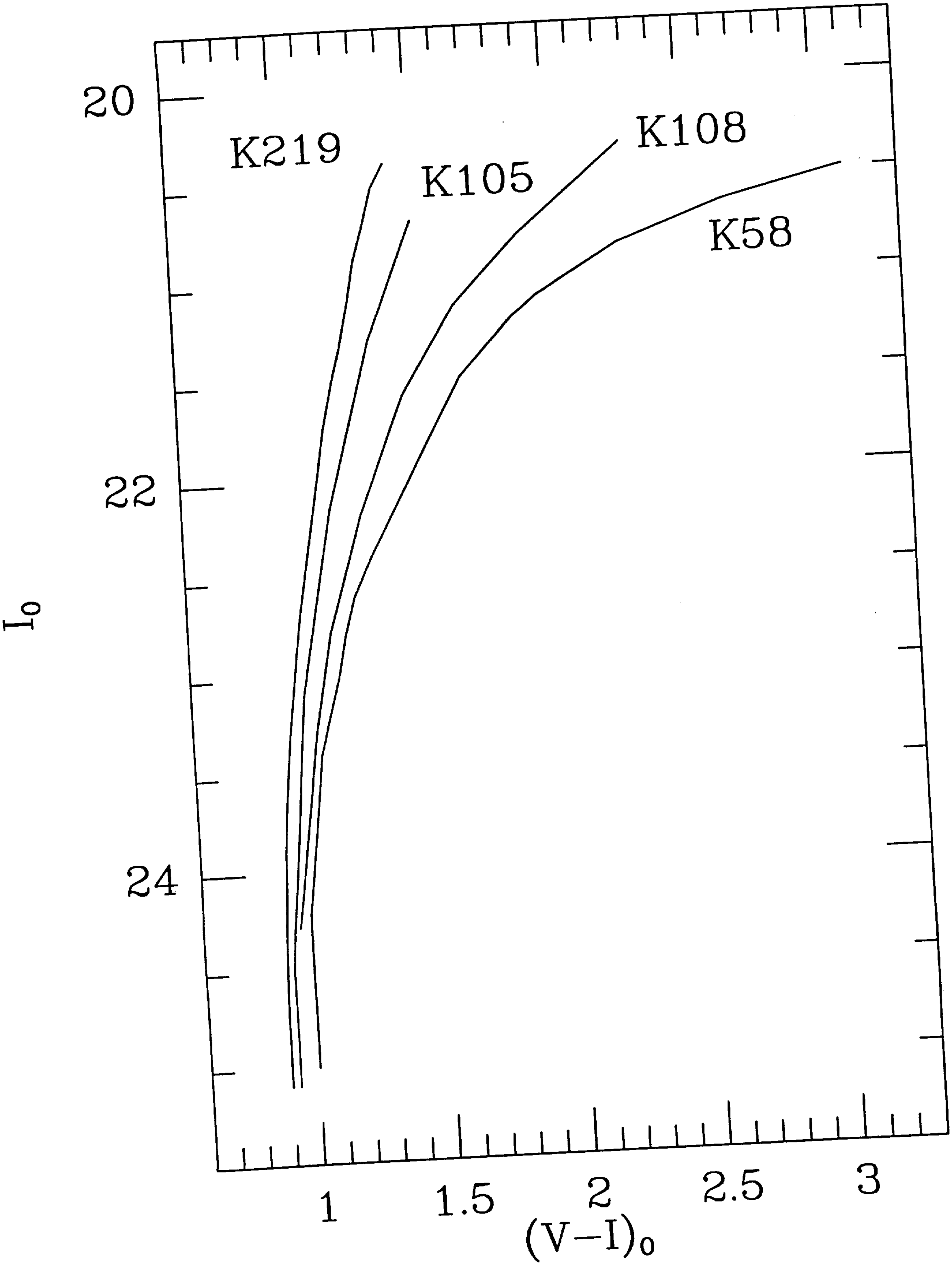

Fig. 24

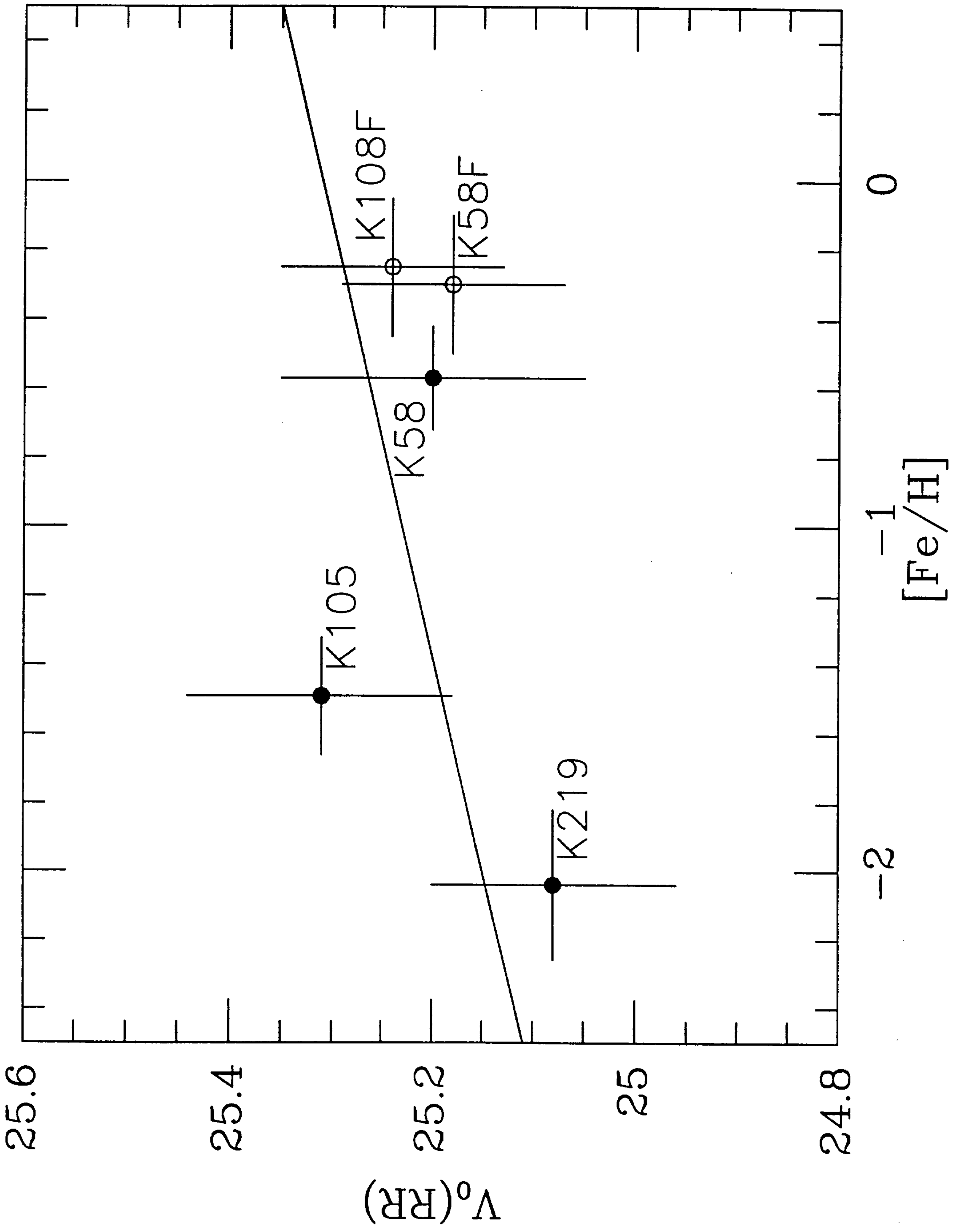Fig. 24